iScience

CellPress
OPEN ACCESS

Article

High-Performance, Large-Area, and Ecofriendly Luminescent Solar Concentrators Using Copper-Doped InP Quantum Dots

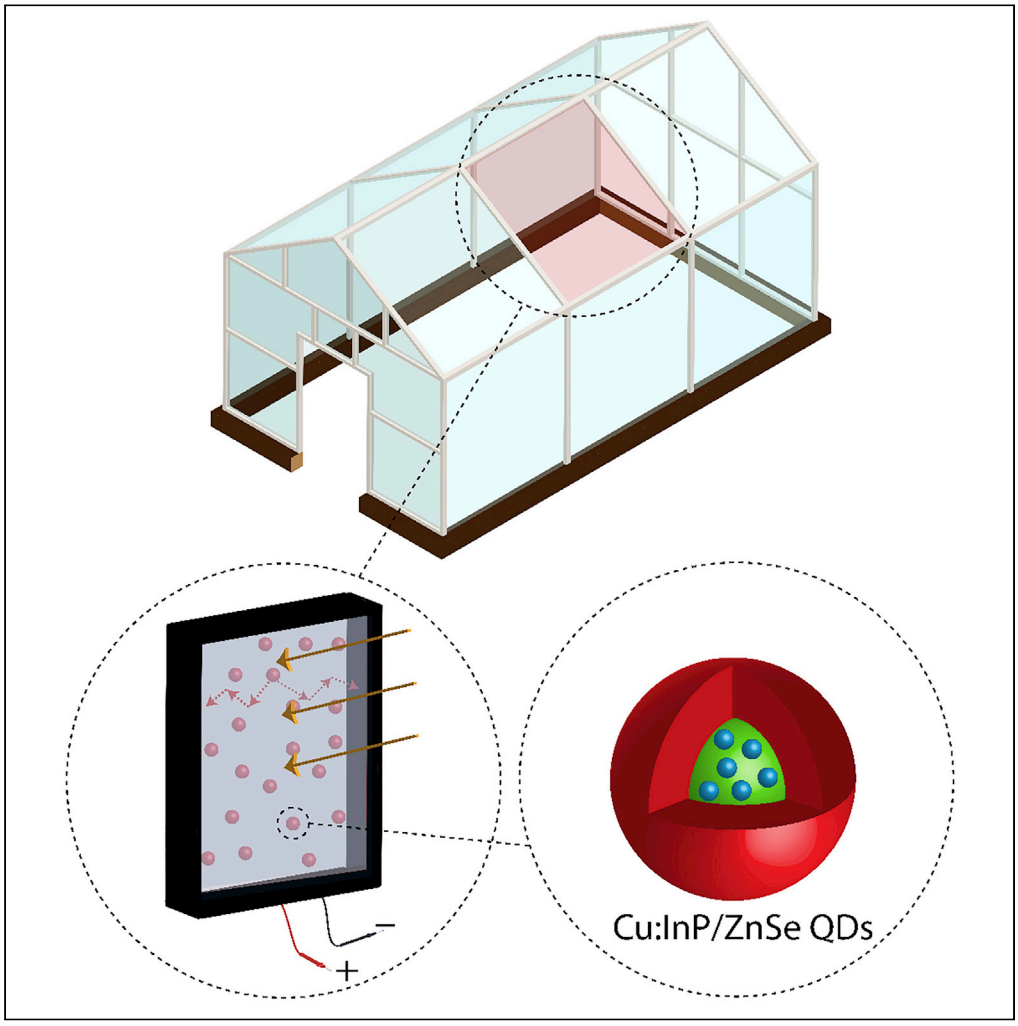

Sadra Sadeghi, Houman Bahmani Jalali, Shashi Bhushan Srivastava, Rustamzhon Melikov, Isinsu Baylam, Alphan Sennaroglu, Sedat Nizamoglu

snizamoglu@ku.edu.tr

HIGHLIGHTS

The luminescent solar concentrators based on copper-doped InP QDs are demonstrated

Efficient excitation transfer led to the exceptionally high in-film PLQY of 81.2%

The LSCs based on copper-doped QDs showed the optical quantum efficiency of 37%

The gram-scale synthesis of QDs led to the fabrication of large-area LSCs (3,000 cm^2)

Sadeghi et al., iScience *23*, 101272
July 24, 2020
https://doi.org/10.1016/j.isci.2020.101272

iScience

CellPress
OPEN ACCESS

Article

High-Performance, Large-Area, and Ecofriendly Luminescent Solar Concentrators Using Copper-Doped InP Quantum Dots

Sadra Sadeghi,[1,6] Houman Bahmani Jalali,[2,6] Shashi Bhushan Srivastava,[3] Rustamzhon Melikov,[3] Isinsu Baylam,[4] Alphan Sennaroglu,[4,5] and Sedat Nizamoglu[1,2,3,7,*]

SUMMARY

Colloidal quantum dots (QDs) are promising building blocks for luminescent solar concentrators (LSCs). For their widespread use, they need to simultaneously satisfy non-toxic material content, low reabsorption, high photoluminescence quantum yield, and large-scale production. Here, copper doping of zinc carboxylate-passivated InP core and nano-engineering of ZnSe shell facilitated high in-device quantum efficiency of QDs over 80%, having well-matched spectral emission profile with the photo-response of silicon solar cells. The optimized QD-LSCs showed an optical quantum efficiency of 37% and an internal concentration factor of 4.7 for a 10 × 10-cm^2 device area under solar illumination, which is comparable with the state-of-the-art LSCs based on cadmium-containing QDs and lead-containing perovskites. Synthesis of the copper-doped InP/ZnSe QDs in gram-scale and large-area deposition (3,000 cm^2) onto commercial window glasses via doctor-blade technique showed their scalability for mass production. These results position InP-based QDs as a promising alternative for efficient solar energy harvesting.

INTRODUCTION

The global demand for electrical energy is increasing each year. According to the International Energy Agency (IEA) report on 2018 (International Energy Agency IEA report, 2018), the worldwide electrical energy consumption showed significant increase in the last 10 years from 18,000 TWh in 2008 to approximately 24,000 TWh in 2018. Today the majority of the global electricity production is done by using fossil fuels, which drastically increases the air pollution and greenhouse gas emission with significant side effects (e.g., global warming, extinction of species, and public health). Despite its great advancements during the recent years, the contribution of the solar energy is limited to only 1.8% (450 TWh) (Bergren et al., 2018), which remained far below its great potential as being one of the most abundant form of "green" energy.

Semi-transparent luminescent solar concentrators (LSCs) offer simple and cost-effective solar energy harvesting solutions to boost the solar energy contribution to global electricity production. LSCs are made of fluorescent materials embedded inside transparent optical waveguides. Fluorescent materials absorb the incoming solar radiation impinging on a large area and convert it to longer-wavelength radiation, and the down-converted light is then guided to the small-area solar cells placed at the edges of the waveguide. The concentration of light by luminescence leads to a significant increase of energy production for the same area of solar cells (Meinardi et al., 2014, 2017a, 2017b; Wu et al., 2018). Therefore, this approach provides a practical energy harvesting solution that can be broadly used as "solar windows" in buildings, vehicles, and roofs (Figure 1).

For its wide-spread use, LSC technology needs to be transformed such that it can simultaneously satisfy efficiency, biocompatibility, and feasibility for large-volume production. More specifically, the following challenges need to be simultaneously addressed: (1) high photoluminescence quantum yield (PLQY) of fluorescent material in its synthesis batch, (2) high quantum efficiency (QE) of them in host matrix, (3) low overlap between the absorbance and photoluminescence (i.e., reabsorption) of the fluorophore, (4) well-matched spectral profile between the photoluminescence of the fluorescent material with the photo-response of the solar cells, (5) being free of toxic elements, and (6) scalable production for wide-spread

[1]Graduate School of Materials Science and Engineering, Koç University, Istanbul 34450, Turkey

[2]Department of Biomedical Sciences and Engineering, Koç University, Istanbul 34450, Turkey

[3]Department of Electrical and Electronics Engineering, Koç University, Istanbul 34450, Turkey

[4]Koç University Surface Science and Technology Center (KUYTAM), Koç University, Istanbul 34450, Turkey

[5]Laser Research Laboratory, Departments of Physics and Electrical-Electronics Engineering, Koç University, Istanbul 34450, Turkey

[6]These authors contributed equally

[7]Lead Contact

*Correspondence: snizamoglu@ku.edu.tr

https://doi.org/10.1016/j.isci.2020.101272

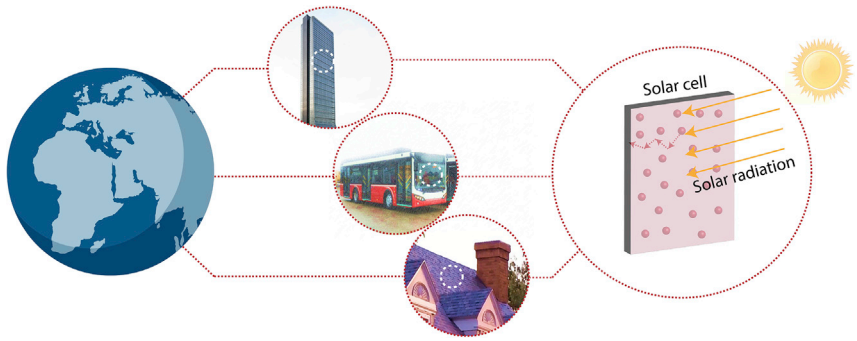

Figure 1. Schematic Representation of Widespread Usability of Luminescent Solar Concentrators (LSCs) in Buildings, Vehicles, and Roofs as "Solar Windows" That Can Boost the Solar Energy Contribution to Global Electricity Production

The fluorescent particles absorb the sunlight and re-emit photons, which are guided through the glass substrate by total internal reflection (TIR) and collected by the solar cells coupled to the edges.

use. Optical quantum efficiency of an LSC is a key efficiency-related figure of merit (Wei et al., 2019) defining the ratio of the output photons, which are extracted from the edges of the LSC to the total number of absorbed photons by the LSC. In order to reach a high optical quantum efficiency level, simultaneous satisfaction of (1)–(3) is required. In addition, (4) allows for efficient conversion of luminescence to electricity, (5) ensures minimum adverse effects of LSCs on environmental sustainability, and (6) shows their ability for large-scale production. Therefore, fulfilling the requirements (1)–(6) can lead to an efficient, ecofriendly, and practical LSC technology for safe and effective solar energy harvesting.

Fluorophores inside the transparent medium are the key building blocks of the LSCs. To date, different types of fluorophores have been employed in LSC structures such as organic dyes (Liang et al., 2004), fluorescent proteins (Sadeghi et al., 2019b), lanthanide-based materials (Graffion et al., 2011), and perovskites (Wei et al., 2019). However, the use of each type of these fluorophores is accompanied with major challenges. Organic dyes have low stability and PLQY when integrated into host materials (Zhou et al., 2018). Fluorescent proteins, despite their unique bio-compatibility and even edibility, similarly suffer from the low PLQY in solid state, which leads to high optical losses (Sadeghi et al., 2019b, 2020). Lanthanides show low absorption coefficient and their compounds are expensive, which are not appropriate for their wide-spread use (Graffion et al., 2011; Nolasco et al., 2013). Perovskites show limited operational lifetime for LSCs (Li et al., 2020; Wei et al., 2019).

Alternatively, colloidal quantum dots (QDs) offer exceptional optoelectronic properties for LSCs. They allow the control of the optical properties by tuning their size, shape, and chemical composition (Bahmani Jalali et al., 2019b; Grabolle et al., 2009; Huang et al., 2015; Kagan et al., 2016). By using different inorganic core/shell structures, high PLQY can be reached to decrease the optical losses (Sharma et al., 2017). The ability of precisely tailoring the absorbance and emission of the QDs can enable low reabsorption losses, which is important to efficiently deliver the down-converted light to solar cells (Meinardi et al., 2014). Moreover, the photo/chemical stability of the QDs can be optimized for long-term use (Kim et al., 2016; Regulacio and Han, 2010; Zhao et al., 2014; Zheng et al., 2019). Therefore, QDs are highly promising candidates for LSC applications.

One compelling material design of QDs is Stokes shift engineering that can suppress reabsorption losses, which is important to minimize the propagation losses of the down-converted luminescence inside the waveguide. Different synthetic procedures have been performed to enlarge the Stokes shift of the QDs such as using indirect band-gap materials (Wang et al., 2017), varying the semiconductor compositions (Bailey and Nie, 2003), growing giant shells (Meinardi et al., 2014), and synthesis of quasi-type II QDs (Meinardi et al., 2014; Sadeghi et al., 2018a). However, QDs produced by these approaches have either toxic heavy-metal content (such as cadmium or lead) or low in-device PLQY. An alternative strategy to engineer the Stokes shift of QDs and enhancing the in-device PLQY can be doping with transition-metal ions (Erickson et al., 2014; Sahu et al., 2012; Viswanatha et al., 2011). Incorporation of small amount of metal impurities (0.1–10 atomic %) as dopants into the host semiconductor QDs introduces new electronic states within the

bandgap (Erickson et al., 2014; Xie and Peng, 2009). The emission from these states is due to the exchange-mediated energy transfer from the photo-excited host semiconductor (Beaulac et al., 2008). Based on the energy level of the metal activator ion, the reabsorption can be effectively suppressed in doped QDs and leads to the Stokes shift up to hundreds of meV (Ronda, 2007; Bryan and Gamelin, 2005). However, the QE of the doped QDs is typically low owing to the slow radiative recombinations, which can be easily outcompeted with the non-radiative processes (Meinardi et al., 2014). Overall, the quest for finding the promising QD candidates, which simultaneously address the above challenges of (1)–(6), is still continuing.

Indium phosphide (InP) QDs, one of the most promising members of QD family for future optoelectronics, showed exceptional efficiency levels for LEDs (Won et al., 2019), photocatalysis (Yu et al., 2018), and neural interfaces (Bahmani Jalali et al., 2018) and also hold high potential for LSCs. Owing to their large exciton Bohr radius (~10 nm) (Tamang et al., 2016) InP QDs are one of the most studied colloidal semiconductor nanocrystals, and their photoluminescence can be sensitively tuned within the visible spectrum via quantum confinement effect. Advantageously, owing to its environmentally benign nature, they are more favorable in comparison with its counterparts containing cadmium and lead elements (Won et al., 2019). Although the optoelectronic properties of InP QDs have been investigated extensively (Tamang et al., 2016), their use for LSCs have been limited owing to their high reabsorption and low efficiency in host materials.

Here, we report LSCs based on synthetically and structurally engineered copper-doped InP QDs that can simultaneously meet the needs of (1)–(6). The synthesized QDs were integrated inside a polydimethylsiloxane (PDMS) polymeric host matrix and deposited on a 10 × 10-cm^2 commercial glass via doctor blade deposition. Owing to efficient excitation transfer from the semiconductor host to the emissive copper ions, photoluminescence in these structures occurs in a nearly reabsorption-free mid-gap region, resulting in an exceptionally high in-film PLQY of 81.2% (Table S2), which led to an optical quantum efficiency of 37% and internal concentration factor of 4.7 for 10 × 10 cm^2 LSCs under the illumination of AM 1.5G solar spectrum. These efficiency levels are comparable with the best previously reported efficiency levels of cadmium-containing QDs and lead-based perovskite nanostructures (Table S5). We further synthesized QDs at gram-scale and fabricated non-toxic, low-loss, and large-area QD-based LSCs with an area of 3,000 cm^2, which can be directly used in buildings and vehicles as the main source of harnessing the solar power to generate electricity. These results position InP-based QDs as a promising alternative for efficient solar energy harvesting.

RESULTS AND DISCUSSION

Synthesis Method and Structural Properties of Copper-Doped InP/ZnSe Core/Shell QDs

We aimed at the synthesis of efficient and bio-compatible QDs with large Stokes shift. For that, first, we synthesized surface-passivated InP cores by hot-injection method (Bahmani Jalali et al., 2019a). Passivation of the InP core was performed by removing the surface dangling bonds using zinc carboxylate (Xu et al., 2008). Zinc carboxylates have the advantages of stable valence state, weak reactivity with phosphorous and low affinity for doping of InP lattice structure, low melting point, high thermal stability at reaction temperature, and non-toxicity (Xu et al., 2008). Moreover, they provide a zinc-rich surface on top of the InP core QDs, which facilitates the growth of additional multi-layer ZnSe shells. Unlike the previous study (Xie and Peng, 2009), which employs indium acetate as the indium precursor, we used indium chloride to form an *in situ* complex with different ligands. Since indium is easily reduced by many Lewis bases, a mixture of hexadecylamine (HDA) and stearic acid (SA) was used to form stable In (III)-ligand complexes. Then, we chemically doped copper ions to the host InP cores by thermal decomposition of copper stearate (Figure 2A). Since the reaction temperature is a key parameter in the successful doping of InP nanocrystals, we added the copper precursor to the reaction at the temperature of 180°C for complete lattice incorporation (Xie and Peng, 2009). Then, for an effective lattice diffusion (Xie and Peng, 2009), the reaction was heated up to 220°C (Figure 2B). The Cu:P precursor ratio was optimized (Figure S4) and the maximum PLQY of 27.6% was obtained at 1% for copper-doped InP core QDs. To decrease the surface defects and increase the PLQY, we choose ZnSe as the shell material since it has lower lattice mismatch with InP (3.4%) (Lim et al., 2011) compared with other commonly used wide-bandgap semiconductors such as ZnS (7.7%) (Lim et al., 2011). By this way, InP can be coated with a thick shell without causing large accumulation of strain. We performed multiple ZnSe shelling up to six monolayers (MLs) by successive ionic layer adsorption and reaction (SILAR) method. The transmission electron microscopy (TEM) analysis indicated that the averaged particle size of InP core (2.5 nm ± 0.2) increased slightly after copper doping (2.7 nm ± 0.2) (Figure 2C).

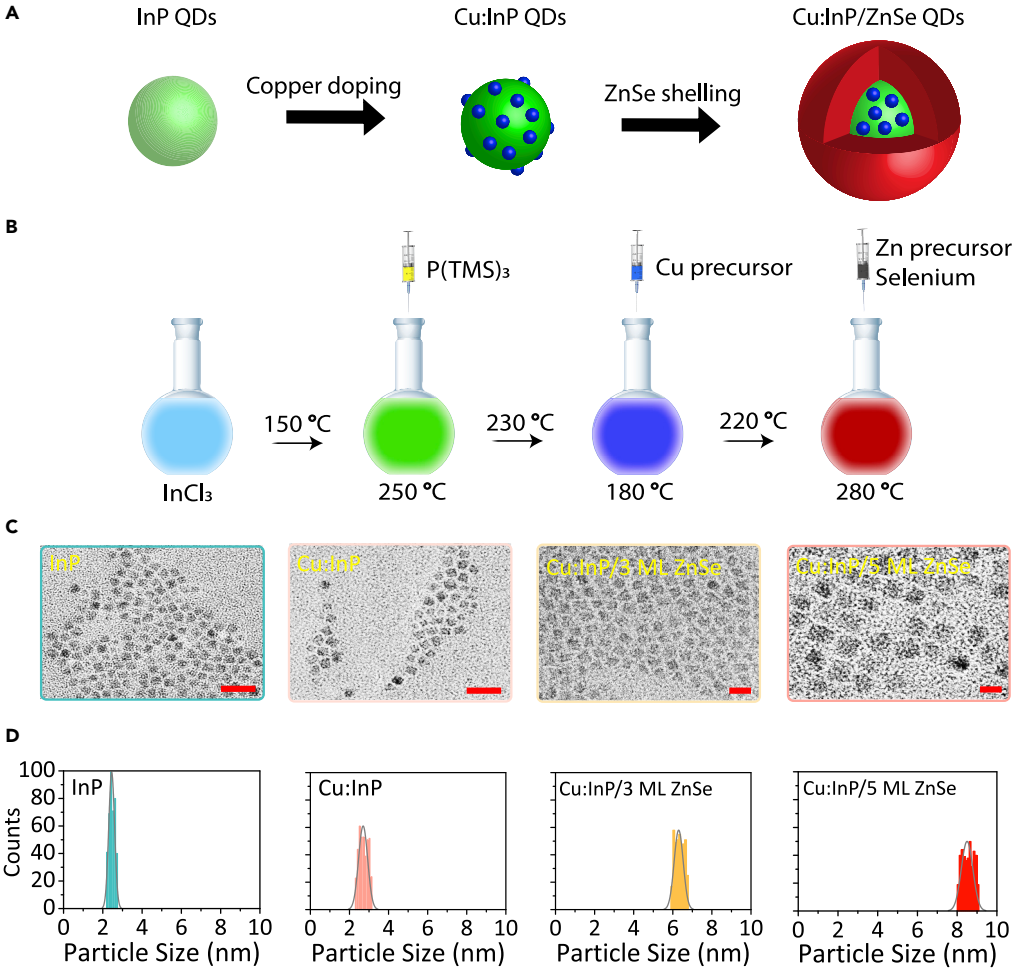

Figure 2. Schematic of the Synthetic Route and Structural Characterization of Copper-Doped InP/ZnSe QDs

(A) After the synthesis of InP core QDs by hot-injection method, core QDs were doped by introducing the copper activator ions. Finally, multiple shelling of ZnSe was performed on the doped InP QDs to increase the PLQY and further suppress the reabsorption.

(B) The synthesis of the InP core QDs was performed by hot injection of the phosphorous precursor ($P(TMS)_3$) to indium precursor ($InCl_3$). After the formation of the InP QDs, the copper precursor was introduced to the reaction, which caused the color change of the solution. Finally, the growth of the ZnSe shell was conducted by injection of the zinc and selenium precursors to the reaction batch via SILAR method.

(C and D) (C) TEM and (D) size distribution of the synthesized QDs. By increasing the shell thickness from 0 to 5 ML, the size of the synthesized QDs increased from 2.5 nm for InP QDs to 8.5 nm for copper-doped InP/5 ML ZnSe QDs. Scale bar for InP and Cu:InP QDs is 5 nm, and scale bar for Cu:InP/3 ML and Cu:InP/5 ML ZnSe QDs is 10 nm. The size distribution of the particles was performed for 400 particles in each TEM image.

After ZnSe shelling, the QDs were enlarged to 6.3 ± 0.2 (for 3 ML ZnSe) and 8.5 ± 0.3 nm (for 5 ML ZnSe). Since each monolayer of ZnSe shell with cubic crystal structure represents 0.57 nm (Ippen et al., 2012), full monolayer coverage was seen in multiple shelling (Figures 2D and S1–S3 and Table S1).

Optical Properties of Copper-Doped InP/ZnSe QDs

To determine the nanostructure with low reabsorption and high efficiency that is suitable for LSC applications, we investigated the optical properties of the synthesized QDs. We performed time-resolved photoluminescence (TRPL) decay measurements of the InP core and copper-doped InP/5 ML ZnSe. The PL decay of the InP core is described by a biexponential decay due to the insufficient surface passivation. The contribution of the fast decay components was decreased by multiple ZnSe shelling, which supports the decrease of the non-radiative components (Figure 3E) (Sharma et al., 2017). In addition, we observed

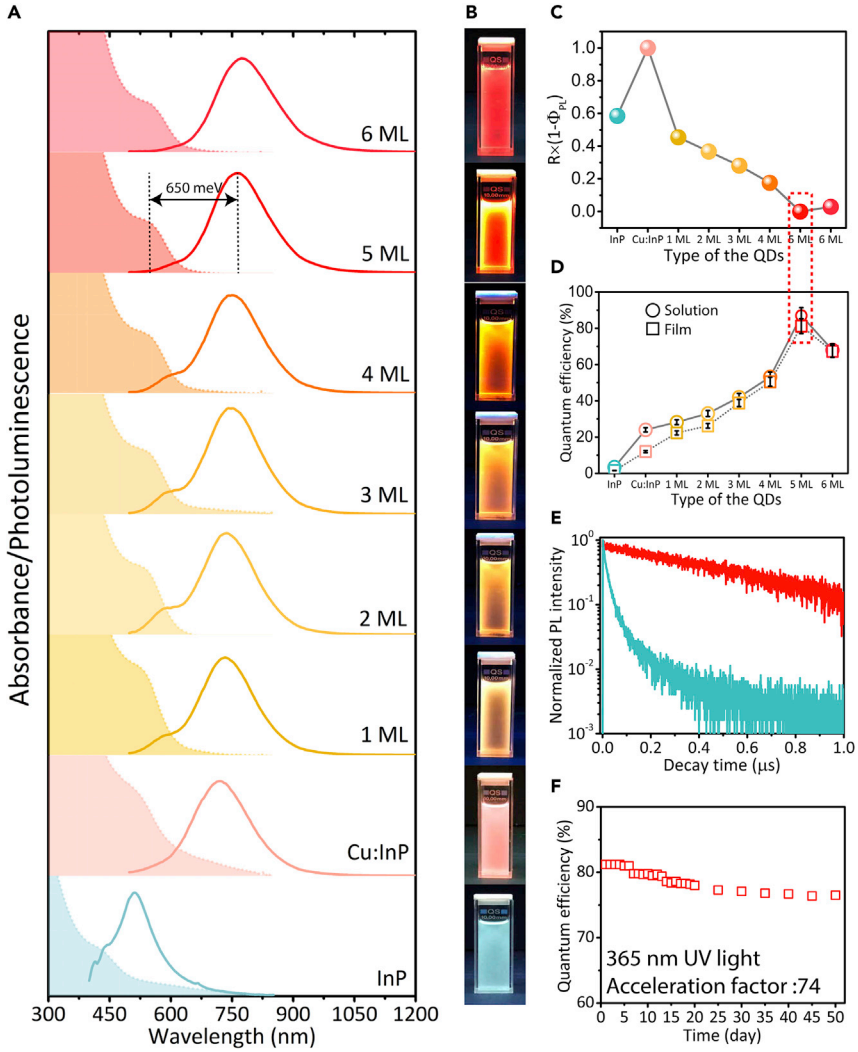

Figure 3. The Optical Properties of Copper-Doped InP/ZnSe QDs

(A) The evolution of the absorbance and photoluminescence spectra of the core InP, copper-doped InP, and copper-doped InP QDs with different ZnSe shell thicknesses ranging from 1 to 6 ML. The absorbance range for each panel was from 0 to 0.1.

(B) The photograph of the synthesized QDs under 365 nm UV irradiation.

(C) Normalized quenching factor of the copper-doped InP QDs calculated by multiplication of reabsorption (R) and (1-Φ_{PL}).

(D) The evolution of the PLQY by increasing ZnSe shell thickness from 0 to 6 ML. The average PLQY increased from 3.4% for InP QDs to 87% for copper-doped InP/5 ML ZnSe QDs in hexane (circles). The similar behavior was also observed in the PLQY of the QDs when embedded inside the polymeric matrix of PDMS (squares) as the average QE of the QDs was increased from 1.5% for InP to 81.2% for copper-doped InP/5 ML ZnSe QDs. Owing to the low reabsorption and high QE, the copper-doped InP/5 ML ZnSe is an appropriate nanostructure for LSCs (red dashed rectangular in (C) and (D)). (The error bars were calculated by the standard error of mean of three samples.)

(E) Time-resolved PL measurements of the InP core and copper-doped InP/5 ML ZnSe QDs in hexane. The copper doping increased the fluorescent lifetime decay significantly from 45 ns for InP to 292 ns for copper-doped InP/5 ML ZnSe owing to the introduction of the localized states by the copper ions.

(F) The accelerated-aging test performed by the excitation of the copper-doped InP/5 ML ZnSe QD film at 365 nm UV irradiation.

that, after copper doping, InP QDs experienced a significant PL redshift of 0.72 eV that leads to a substantial decrease of the reabsorption (Figures 3A and 3B). Furthermore, the presence of copper dopant centers located in the interior of the copper-doped InP core upon lattice diffusion leads to higher PLQY in

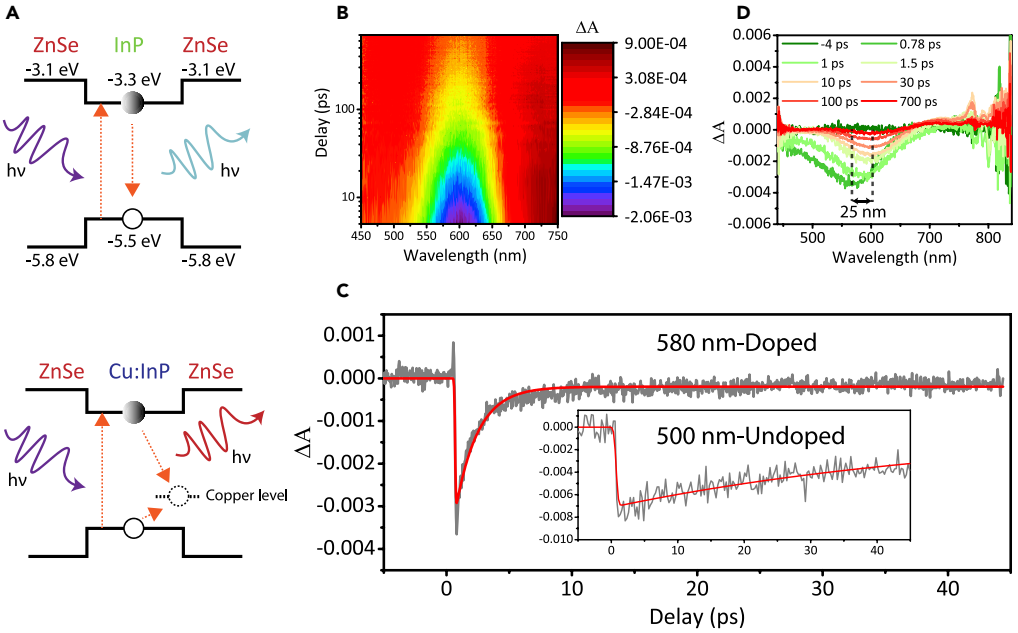

Figure 4. Band Diagram and Ultrafast Non-linear Absorption Spectroscopy of the Copper-Doped InP/5 ML ZnSe QDs

(A) The energy band diagram of the undoped (upper panel) and copper-doped (lower panel) InP/ZnSe QDs. In undoped QDs, the photon is absorbed and interband recombination takes place. When QDs are doped with copper, mid-gap states are introduced, which are responsible for the red shift in emission.

(B) The contour plot showing the measured ΔA of the copper-doped InP/ZnSe QDs as a function of probe delay and wavelength.

(C) Time-resolved ΔA response of the copper-doped InP/ZnSe QDs at the probe wavelength of 580 nm. The decay lifetimes of the copper-doped QDs were determined as 0.9 and 6.3 ps. Inset: Time-resolved ΔA response of the undoped InP/ZnSe QDs at the probe wavelength of 500 nm with the decay lifetimes 2.4 and 25.5 ps.

(D) The measured ΔA spectra of the QDs at eight selected probe delays ranging from −4 ps to 700 ps. The excitation wavelength was 400 nm.

comparison with the intrinsic InP cores (Xie and Peng, 2009). Via the growth of ZnSe shell, the emission and absorption bands were further separated and led to the significant Stokes shift up to 650 meV (the difference between the PL peak at 1.62 eV and the absorption broad shoulder at 2.27 eV) and suppression of reabsorption (Figure 3A). In addition to the decrease of reabsorption, the shell growth isolates the surface traps and effectively confines the electron-hole wave functions inside the nanostructure, which leads to the increase of the PLQY. To select the appropriate nanostructure for LSC, the quenching factor (i.e., reabsorption × (1-Φ_{PL})) was calculated for different ZnSe shell thicknesses (Figure 3C) and the minimum of the quenching factor was observed for five MLs. The maximum PLQY of QDs in hexane solution was observed as 87% ± 4 for five monolayers of ZnSe shell formation (Figures 3D and S5). Hence, considering the quenching factor and PLQY, we selected copper-doped InP/5 ML ZnSe as the optimum sample for LSC fabrication. To investigate the photo-stability of the QDs in-film, their quantum efficiency was measured by accelerated-aging test under 365 nm illumination (see Transparent Methods) and showed only 5.8% decrease (from 81.2% to 76.5%) in 50 days (Figure 3F).

The Non-linear Absorption Spectroscopy of the Copper-Doped QDs

To further investigate the nature of the Stokes shift in the synthesized copper-doped QDs and understand the emission mechanisms (Figure 4A), the non-linear absorption and ultrafast decay properties of the copper-doped and undoped InP/5 ML ZnSe QDs were further investigated by using a femtosecond pump-probe spectrometer (Baylam et al., 2019). QD solutions were excited at 400 nm at a fluence of 135 $\mu J.cm^{-2}$, and the difference between the absorbance of the pumped and unpumped sample ($\Delta A = A_{pumped}-A_{unpumped}$) was probed by using a femtosecond white light continuum ranging from 450 to 800 nm (Figures 4B and S16). The ΔA peak wavelength of the undoped QDs remains almost identical to the absorbance shoulder of the QDs at 556 nm (2.23 eV), showing that the interband transitions are

responsible for the transitions in the undoped samples (see Figure S17). The ultrafast transient evolution of the nonlinear absorbance (Figure 4C) was analyzed by employing a biexponential decay fit consisting of decay times τ_1 and τ_2. Similar to what was reported in earlier investigations (Dutta et al., 2018; Peng et al., 2010), the decay times τ_1 and τ_2 describe fast decay due to intermediate trapping states. In addition, as can be seen from Figure 4B, ΔA remains non-zero beyond a probe delay of 700 ps, due to interband electron-hole recombination that occurs over nanosecond time scales. The latter transition rates are determined from luminescence decay measurements described in Figure 3E. The measured ultrafast decay times of copper-doped QDs (τ_1 = 0.9 ps, τ_2 = 6.3 ps) at the probe wavelength of 580 nm (Figure 4C) are considerably shorter than those for undoped QDs (τ_1 = 2.4 ps, τ_2 = 25.5 ps, probe wavelength of 500 nm, see inset of Figure 4B) owing to copper-induced mid-gap states. In addition, the peak wavelength of the ΔA spectrum of the doped QDs shifted from 566 (2.19 eV) to 591 nm (2.09 eV) over a delay of 1.5 ps (Figure 4D). The pump fluence was relatively low (the estimated average number of generated electron-hole pairs corresponded to $<N>\sim0.5$) for the observation of a Stark effect-induced spectral change, and at the same fluence level no spectral variation was observed for the undoped QDs. Hence, we attributed that the copper dopants in InP/5 ML ZnSe QDs play the role as an "extra" hole acceptor level (Knowles et al., 2016).

Low-Loss InP-Based QD-LSCs

We fabricated copper-doped InP/ZnSe QD-based LSCs by doctor-blade deposition of QD-polymer mixture (d = 100 μm) onto the glass substrates (D = 2 mm) (Figure 5A). We selected PDMS elastomer as the polymeric host matrix that is highly transparent both in the visible and near-IR region (Wang et al., 2016) and offers inexpensive large-scale production (Sackmann et al., 2014; Sadeghi et al., 2018c, 2019a). Despite the favorable properties of PDMS, in fact, the initiator radicals of such polymers can interact with QDs and increase the non-radiative channels (Sadeghi et al., 2018a). This has the risk of significantly decreasing the QE of QDs. For example, in previous reports, a QE decrease of 50% is observed (Sadeghi et al., 2018b), which can be solved by special methods such as cell casting (Meinardi et al., 2014). Noticeably, without any special treatment of PDMS, we observed strong photoluminescence of QDs in regular PDMS films with only a ~6% QE decrease with respect to the solution due to the strong confinement of photo-generated charge carriers via the sufficiently thick ZnSe shell (Figures 3D and 5C). The total internal reflection of the photoluminescence was especially visible at the edges of the waveguide (Figure 5C). The QD layer in the fabricated QD-LSC showed a small PL peak wavelength change from 767 nm in solution to 772 nm in film, respectively (Figure 5D). Advantageously, the thin film deposition of QD-polymer layer preserves the transparency of the fabricated QD-LSCs, which is critical for indoor and outdoor solar window applications (Figure 5B). The absorbance of the QD-LSC at the first excitonic peak was measured as 0.093 (Figure 5D), equal to the high transmission level of 81%, which was also observable in the photograph of QD-LSC slab under ambient light (Figure 5B). The small offset (0.05) in the absorbance of the device (dashed line in Figure 5D) is due to the light reflection from the LSC (equal to ~11% reflectivity).

To evaluate the suitability of the copper-doped InP/5 ML ZnSe QDs in LSC panels, the optical properties of the fabricated QD-based LSC with the dimensions of 10 × 10 cm^2 were investigated. To simulate the situations in which the solar window panels are illuminated partially by sunlight irradiation on the different hours of the day, the portion of the illumination area under UV light was altered (Figure 5E inset). As illumination area increased from 0 to 100 cm^2 (equal to the full length of LSC at 10 cm), the optical output intensity increased with a linear slope owing to the effective suppression of the reabsorption by QDs (Figure 5E). At the same time, the emission spectra of the QDs at different illumination area showed almost no significant spectral peak position change ($\Delta\lambda$ = 4 nm), demonstrating the low reabsorption of the LSC under different areal illumination conditions (Figure 5F), and the emission spectrum also matched well with the spectral response of silicon photovoltaic cells for efficient light harvesting (Figure S7). For direct evaluation of the reabsorption in the fabricated QD-LSC, laser light at 365 nm was used to excite the face of QD film and the output intensity was recorded from the edge at different optical distances from the excitation spot (Figure 5G inset). The normalized integrated PL intensity decreased by 21% by increasing the optical distance up to 10 cm (Figures 5G and 5H). This trend mainly originates from the reabsorption and scattering losses. To figure out the scattering losses, we investigated experimentally by propagating a laser beam through the edge of the fabricated QD-based LSC at the wavelength of 780 nm, where QDs have negligible absorption (Figure 5D). The output light was collected at different optical distances from the illumination edge by using an optical fiber (Figure S9). By increasing the light

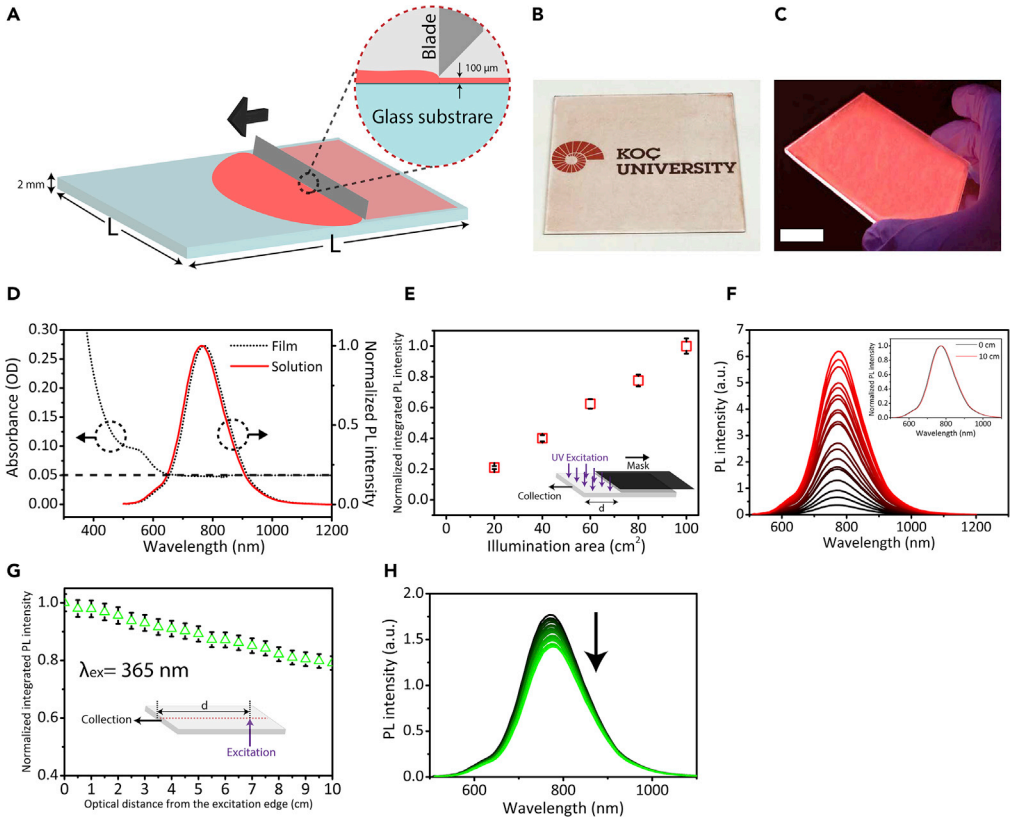

Figure 5. Copper-Doped InP/ZnSe QD-Based LSCs

(A) Schematic representation of the fabrication process. After mixing the QD solution with PDMS elastomer and degassing, the mixture was poured onto a glass substrate. Then, by using the doctor blade, a thin film with the thickness of 100 μm was formed on the glass.

(B) The transparency of the fabricated LSC with the loading concentration of 26 mg.mL^{-1} was shown under ambient light.

(C) Photograph of the QD-based LSC under 365 nm UV irradiation. The total internal reflection is visible on the edges as they seemed brighter (scale bar, 1 cm).

(D) Absorbance and PL of the QDs in the film (black dashed line) with the loading concentration of 26 mg.mL^{-1} and in solution (red line).

(E) The optical output intensity of the 10 × 10 cm^2 QD-based LSC by changing the illumination area from 0 to 100 cm^2. Inset: Schematic of the setup to change the portion of the illuminated area of LSC under UV radiation.

(F) The output emission spectra of the LSC, when illumination area increased as in (E). Inset: Normalized output spectra at the optical distances of 0 and 10 cm from the collection edge.

(G) The spectrally integrated output of QD-based LSC under the illumination by a UV laser beam at 365 nm wavelength. Inset: Laser beam excitation was perpendicular to the surface with different optical distances and the light was collected at the slab edge.

(H) The output emission spectra of the LSC, when the optical distance from the excitation point and the collection edge was increased as in (G). (The error bars were calculated by the standard error of mean for three measurements.)

collection distance up to 10 cm, the output intensity corresponds to a scattering loss of 0.016 cm^{-1} (Figure S9B). By including the scattering term in the PL decay (Figure 5G), the effective reabsorption coefficient corresponds to 0.004 cm^{-1} (Figure S8), showing that the reabsorption was significantly suppressed.

We characterized and analyzed the efficiency of the copper-doped QD-based LSCs. To investigate the effect of LSC size, we fabricated QD-LSCs with the dimensions of 5 × 5, 10 × 10, and 20 × 20 cm^2 having loading concentration of 26 mg.mL^{-1}. At the same time, we fabricated two separate LSCs with the same dimension of 10 × 10 cm^2 having different loading concentrations of 13 and 52 mg.mL^{-1} (Figure S7). QD-LSCs were illuminated orthogonal to the front surface by a calibrated AM 1.5G solar spectrum (Figure S10), and the photoluminescence generated by the QDs was coupled to the silicon solar cell positioned on the collection edge (see Transparent Methods).

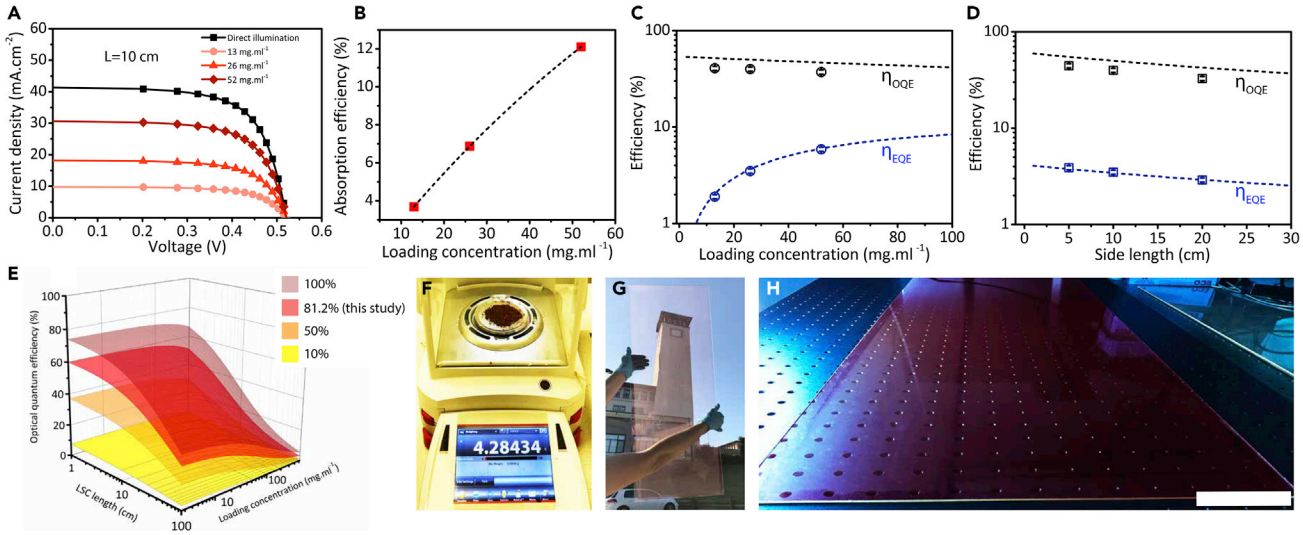

Figure 6. Large-Area Copper-Doped InP/ZnSe QD-Based LSCs and Evaluation of Optical Quantum Efficiency of Fabricated Devices

(A) The J-V curves of the silicon solar cells coupled to the QD-LSCs with the LSC length of 10 cm at different loading concentrations of 13, 26, and 52 mg.mL^{-1} under the illumination of AM 1.5G solar simulator. The J-V curve of the silicon solar cell under direct illumination of the solar simulator was also shown (black line).

(B) The absorption efficiency values for different loading concentration of the QDs. The dashed line and the points represent the simulated and experimental results, respectively.

(C and D) (C) The simulated (dashed line) and experimental (symbols) values of optical and external quantum efficiency for the QD-LSCs with different loading concentration of the QDs ranging from 13, 26, and 52 mg.mL^{-1} and (D) different side lengths of 5, 10, and 20 cm.

(E) The simulation of the optical quantum efficiency of QD-LSCs having different QE of QDs ranging from 10%, 50%, 81.2% (QE of this study) and unity at different LSC lengths ranging from 1 to 100 cm and different loading concentration between 2.6 and 520 mg.mL^{-1}.

(F) Up-scaled amount of copper-doped InP/ZnSe core/shell QDs after single synthesis.

(G) The fabricated large-area QD-based LSC under sunlight irradiation with the dimensions of 100 × 30 cm^2.

(H) The large-area LSC under weak UV illumination (scale bar, 5 cm).

In order to measure the optical quantum efficiency of the fabricated LSCs, the expression $\eta_{OQE} = (J_{LSC}A_{PV})/(J_{PV}A_{LSC}\eta_{abs}q_{LSC}\eta_{coupling})$ (Wei et al., 2019) was used, where J_{LSC} is the short-circuit current of the solar cell coupled to the LSC when LSC is illuminated by the solar simulator, J_{PV} is the short-circuit current of the solar cell when the solar cell is directly illuminated by the solar simulator without LSC, q_{LSC} is the reshaping factor equal to 1.73, η_{abs} is the absorption efficiency dependent on the loading concentration of the QDs (Figure 6B), and $\eta_{coupling}$ is the PL coupling efficiency from the LSC to the solar cell, which is calculated as 75.2% (see Supplemental Information) (Wu et al., 2018). Based on the electro-optical characterizations, J_{LSC}/J_{PV} values measured as 0.24, 0.44, and 0.74 for the loading concentration of 13, 26, and 52 mg.mL^{-1}, respectively (Figure 6A), which resulted in the optical quantum efficiency of QD-LSCs of 40.7%–39.9% and 37.2% for a 10 × 10 cm^2 area, respectively (Figure 6C). When the side length of LSC changed to 5 and 20 cm at 26 mg.mL^{-1}, J_{LSC}/J_{PV} values of the QD-LSCs were shifted 0.24 and 0.73, respectively (Figure S15). But, at the same time, since the G factor increased from 6.25 to 25, the optical quantum efficiency of the QD-LSC with different LSC lengths led to 44.3% and 32.7%, respectively (Figure 6D and Table S4). The observed optical quantum efficiency levels are as a result of high in-film QE of the QDs, suppressed reabsorption due to the separation of absorption and emission centers (Stokes shift > 600 meV), and the high optical quality of the fabricated films mitigating the propagation-loss problem. To the best of our knowledge, the optical quantum efficiencies of the more environmentally benign InP-based LSCs have comparable efficiency levels with the best Cd- and Pb-based LSCs (Table S5). Table S5 shows that Si and CuInS QDs have high potential for future LSCs as well.

Besides, the optical quantum efficiency of the InP QD-LSC having 52 mg.mL^{-1} led to a high internal concentration factor calculated by $CF_{int} = G \times \eta_{OQE}$ (Wei et al., 2019), which corresponds to 4.7 for the LSC panels with the dimensions of 10 × 10 cm^2. The external quantum efficiency of the LSC is defined as the ratio of the number of the photons reaching to the coupled solar cell to the total number of the input photons. As a result of electro-optical measurement, the concentration of 52 mg.mL^{-1}

achieved the highest external quantum efficiency of 5.9% owing to high absorption efficiency in comparison with the other LSCs having different concentration levels (Figures 6C and 6D). These external quantum efficiencies are also in agreement with the simulations based on $\eta_{EQE} = \eta_{abs}\eta_{OQE}q_{LSC}\eta_{coupling}$ (Figures S11–S13 and Table S3). Moreover, the solar-to-electrical power conversion efficiency (i.e., PCE_{LSC}) corresponds to 0.9% by using a stand-alone solar cell that has an efficiency of 14.5%, respectively (Figure S14).

To understand the ultimate efficiency levels achievable by the QD-LSCs, we performed the simulation of the optical quantum efficiency by considering QEs of 10%, 50%, 81.2% (this study), and 100%, with the LSC length and loading concentration ranging from 1 to 100 cm and from 2.6 to 520 $mg.mL^{-1}$, respectively (Figure 6E). By increasing the QE of the QDs to unity, the ultimate optical quantum efficiency levels of QD-LSCs can reach up to 70% for an area of 10 × 10 cm^2, while keeping sufficient level of transmittance more than 50% in the eye sensitivity peak (λ = 555 nm). Thus, the optical quantum efficiency of 70% can push up the external quantum efficiency to the maximum value of ~14% while a refractive index-matching polymer between LSC and PV module is used and a moderate absorption efficiency of 20% is assumed. If a more efficient solar cell module (having 23.7%) (Wu et al., 2018) would be used for optical quantum efficiency of 70%, the power conversion efficiency could be further increased up to ~3.3% under the standard AM 1.5G solar illumination. In addition, integration of lower-band gap QDs emitting at 900–1,000 nm matching with the responsivity of the silicon solar cells can significantly boost the power conversion efficiency levels. Furthermore, the use of reflectors on the bottom of the LSC can increase the power conversion efficiency though decreasing the transparency.

Scalability of Copper-Doped InP QDs for Large-Area and Wide-Spread-Usable LSCs

In order to fabricate large-area QD-based LSCs, the amount of QDs needs to be scaled up to a sufficient level. For that, we increased the reaction yield up to 4.28 g of the copper-doped InP/5 ML ZnSe QDs in one reaction batch (Figure 6F) (see Transparent Methods for detailed amounts of precursors and synthetic procedure). To assess the applicability of the fabricated LSCs to large-area solar window applications, the synthesized copper-doped QDs with the concentration of 26 $mg.mL^{-1}$ were mixed with the polymer and deposited on 100 × 30 cm^2 glass substrate by using doctor-blade technique (Figures 6G and S6). Regardless of the size and the high loading concentration of the QDs in the large-area device (26 $mg.mL^{-1}$), the fabricated devices are highly transparent under sunlight irradiation (Figure 6G). At the same time, the UV illumination of the large-area QD-based LSC led to strong emission from all parts of the fabricated device, indicating the feasibility for large-area LSC operation and fabrication (Figure 6H).

Conclusions

In this study, we showed that indium phosphide (InP)-based QDs are a promising candidate for future LSC technology that can simultaneously fulfill the requirements of the efficiency, eco-compatibility, and large-scale production. The Stokes shift of the InP QDs was realized by copper doping (650 meV), and the PLQY of the synthesized QDs was boosted up to 87% in the "near-infrared window" by passivation of surface traps via zinc carboxylation and strong confinement of electron-hole pairs inside the nanostructure via growing lattice-matched ZnSe shell. Moreover, the high PLQY over 80% is also maintained in solid-state form owing to the thick ZnSe shell. The high PLQY and low reabsorption facilitated high optical quantum efficiencies over 30%, comparable with the best reported Cd and Pb-containing LSCs. By using the doctor-blade technique, a large-area QD-based LSC (3,000 cm^2) was fabricated, which indicates the applicability for "solar window" applications. Moreover, incorporation of QDs having QE of 100% into LSCs can lead to power conversion efficiency levels above 3%. Collectively, this work demonstrates a significant step forward toward the realization of ecofriendly, efficient, and large-area LSCs, which show remarkable potential to be widely used for solar-powered buildings and vehicles in the near future.

Limitations of the Study

In this study, we report LSCs based on synthetically and structurally engineered copper-doped InP QDs that can simultaneously meet the needs of high efficiency, being free of toxic elements and scalability. The synthesized QDs were integrated inside a polydimethylsiloxane (PDMS) polymeric host matrix and deposited on a 10 × 10 cm^2 commercial glass via doctor blade deposition. Owing to efficient excitation

transfer from the semiconductor host to the emissive copper ions, photoluminescence in these structures occurs in a nearly reabsorption-free spectral region. Moreover, they have high in-film PLQY of 81.2%, which led to an optical quantum efficiency of 37% and internal concentration factor of 4.7 for 10 × 10 cm^2 LSCs under the illumination of AM 1.5G solar spectrum. The current study, however, falls short to reach the external quantum efficiency more than 10% owing to the low efficiency of the silicon solar cells used for the electro-optical measurements. Moreover, the optical stability of the fabricated QD-LSCs has only been tested under UV light. For better accuracy, it is better to evaluate them under sun irradiation or other broadband light sources under different humidity levels. In addition, the distribution of copper dopant inside the core/shell structure can provide more insight about the structural properties. Furthermore, the cost of the PDMS and QD synthesis chemicals may also limit large-scale production. Hence, further studies and optimizations that can address the above issues can improve the understanding of QDs and LSC performance.

Resource Availability

Lead Contact

Further information and requests for resources and reagents should be directed to and will be fulfilled by the Lead Contact, Sedat Nizamoglu (snizamoglu@ku.edu.tr).

Materials Availability

This study did not generate new unique reagents.

Data and Code Availability

The published article includes all datasets/code generated or analyzed during this study.

METHODS

All methods can be found in the accompanying Transparent Methods supplemental file.

SUPPLEMENTAL INFORMATION

Supplemental Information can be found online at https://doi.org/10.1016/j.isci.2020.101272.

ACKNOWLEDGMENTS

S.N. acknowledges the support by the European Research Council (ERC) under the European Union's Horizon 2020 Research and Innovation Programme (Grant agreement no. 639846). S.N. acknowledges the support by the Turkish Academy of Sciences (TÜBA-GEBİP; The Young Scientist Award Program) and the Science Academy of Turkey (BAGEP; The Young Scientist Award Program). The authors thank M. Han for the assistance in the QD-LSC fabrication and measurements. The authors thank the Koç University Tüpraş Energy Center (KUTEM) and Koç University Surface Science and Technology Center (KUYTAM) for the structural analysis of QDs. The auhtors would like to thank Prof. E. Şenses for his helpful discussions on optical measurements of QD-LSCs.

AUTHOR CONTRIBUTIONS

S.N and S.S developed the idea and designed the experiments.. S.S. executed the quantum dot and LSC experiments. H.B.J. synthesized QDs and optimized their optical properties. R.M. and S.S. measured and analyzed the optical performances of LSCs. S.S. and H.B.J. performed the QD characterization. S.S. and H.B.J. performed time-resolved PL and analyzed the data. S.B.S. fabricated the QD-based LSCs with different dimensions and performed the electro-optical measurements. I.B. and A.S. performed the nonlinear absorption spectroscopy and wrote the related discussion. I.B. assisted S.S. in the optical measurements of QD-LSCs. All authors wrote the manuscript and have given approval to the final version of the manuscript.

DECLARATION OF INTERESTS

The authors declare no competing interest.

Received: April 28, 2020
Revised: June 2, 2020
Accepted: June 9, 2020
Published: July 24, 2020

REFERENCES

Bahmani Jalali, H., Mohammadi Aria, M., Dikbas, U.M., Sadeghi, S., Ganesh Kumar, B., Sahin, M., Kavakli, I.H., Ow-Yang, C.W., and Nizamoglu, S. (2018). Effective neural photostimulation using indium-Based type-II quantum dots. ACS Nano *12*, 8104–8114.

Bahmani Jalali, H., Karatum, O., Melikov, R., Dikbas, U.M., Sadeghi, S., Yildiz, E., Dogru, I.B., Ozgun Eren, G., Ergun, C., and Sahin, A. (2019a). Biocompatible quantum funnels for neural photostimulation. Nano Lett. *19*, 5975–5981.

Bahmani Jalali, H., Sadeghi, S., Sahin, M., Ozturk, H., Ow-Yang, C.W., and Nizamoglu, S. (2019b). Colloidal aluminum antimonide quantum dots. Chem. Mater. *31*, 4743–4747.

Bailey, R.E., and Nie, S. (2003). Alloyed semiconductor quantum dots: tuning the optical properties without changing the particle size. J. Am. Chem. Soc. *125*, 7100–7106.

Baylam, I., Cizmeciyan, M., Kakenov, N., Kocabas, C., and Sennaroglu, A. (2019). Ultrafast spectroscopy of voltage reconfigurable graphene saturable absorbers in the visible and near infrared. 2D Mater. *6*, 035013.

Beaulac, R., Archer, P.I., and Gamelin, D.R. (2008). Luminescence in colloidal Mn2+-doped semiconductor nanocrystals. J. Solid State Chem. *181*, 1582–1589.

Bergren, M.R., Makarov, N.S., Ramasamy, K., Jackson, A., Guglielmetti, R., and McDaniel, H. (2018). High-performance CuInS2 quantum dot laminated glass luminescent solar concentrators for windows. ACS Energy Lett. *3*, 520–525.

Bryan, J.D., and Gamelin, D.R. (2005). Doped semiconductor nanocrystals: synthesis, characterization, physical properties, and applications. Prog. Inorg. Chem. *54*, 47–126.

Dutta, A., Bera, R., Ghosh, A., and Patra, A. (2018). Ultrafast carrier dynamics of photo-induced Cu-doped CdSe nanocrystals. J. Phys. Chem. C *122*, 16992–17000.

Erickson, C.S., Bradshaw, L.R., McDowall, S., Gilbertson, J.D., Gamelin, D.R., and Patrick, D.L. (2014). Zero-reabsorption doped-nanocrystal luminescent solar concentrators. ACS Nano *8*, 3461–3467.

Grabolle, M., Spieles, M., Lesnyak, V., Gaponik, N., Eychmüller, A., and Resch-Genger, U. (2009). Determination of the fluorescence quantum yield of quantum dots: suitable procedures and achievable uncertainties. Anal. Chem. *81*, 6285–6294.

Graffion, J., Cattoën, X., Wong Chi Man, M., Fernandes, V.R., André, P.S., Ferreira, R.A., and Carlos, L.D. (2011). Modulating the photoluminescence of bridged silsesquioxanes incorporating Eu3+-complexed n, n′-diureido-2, 2′-bipyridine isomers: application for luminescent solar concentrators. Chem. Mater. *23*, 4773–4782.

Huang, H., Susha, A.S., Kershaw, S.V., Hung, T.F., and Rogach, A.L. (2015). Control of emission color of high quantum yield CH3NH3PbBr3 perovskite quantum dots by precipitation temperature. Adv. Sci. *2*, 1500194.

International Energy Agency (IEA) report, 2018. https://www.ren21.net/wp-content/uploads/2019/05/GSR2018_Full-Report_English.pdf.

Ippen, C., Greco, T., and Wedel, A. (2012). InP/ZnSe/ZnS: a novel multishell system for InP quantum dots for improved luminescence efficiency and its application in a light-emitting device. J. Infect. Dis. *13*, 91–95.

Kagan, C.R., Lifshitz, E., Sargent, E.H., and Talapin, D.V. (2016). Building devices from colloidal quantum dots. Science *353*, aac5523.

Kim, B.H., Nam, S., Oh, N., Cho, S.-Y., Yu, K.J., Lee, C.H., Zhang, J., Deshpande, K., Trefonas, P., and Kim, J.-H. (2016). Multilayer transfer printing for pixelated, multicolor quantum dot light-emitting diodes. ACS Nano *10*, 4920–4925.

Knowles, K.E., Hartstein, K.H., Kilburn, T.B., Marchioro, A., Nelson, H.D., Whitham, P.J., and Gamelin, D.R. (2016). Luminescent colloidal semiconductor nanocrystals containing copper: synthesis, photophysics, and applications. Chem. Rev. *116*, 10820–10851.

Li, Z., Johnston, A., Wei, M., Saidaminov, M.I., de Pina, J.M., Zheng, X., Liu, J., Liu, Y., Bakr, O.M., and Sargent, E.H. (2020). Solvent-solute coordination engineering for efficient perovskite luminescent solar concentrators. Joule *4*, 631–643.

Liang, H., Zheng, Z., Li, Z., Xu, J., Chen, B., Zhao, H., Zhang, Q., and Ming, H. (2004). Fabrication and amplification of Rhodamine B-doped step-index polymer optical fiber. J. Appl. Polym. Sci. *93*, 681–685.

Lim, J., Bae, W.K., Lee, D., Nam, M.K., Jung, J., Lee, C., Char, K., and Lee, S. (2011). InP@ ZnSeS, core@ composition gradient shell quantum dots with enhanced stability. Chem. Mater. *23*, 4459–4463.

Meinardi, F., Colombo, A., Velizhanin, K.A., Simonutti, R., Lorenzon, M., Beverina, L., Viswanatha, R., Klimov, V.I., and Brovelli, S. (2014). Large-area luminescent solar concentrators based on 'Stokes-shift-engineered' nanocrystals in a mass-polymerized PMMA matrix. Nat. Photon. *8*, 392.

Meinardi, F., Bruni, F., and Brovelli, S. (2017a). Luminescent solar concentrators for building-integrated photovoltaics. Nat. Rev. Mater. *2*, 17072.

Meinardi, F., Ehrenberg, S., Dhamo, L., Carulli, F., Mauri, M., Bruni, F., Simonutti, R., Kortshagen, U., and Brovelli, S. (2017b). Highly efficient luminescent solar concentrators based on earth-abundant indirect-bandgap silicon quantum dots. Nat. Photon. *11*, 177–185.

Nolasco, M.M., Vaz, P.M., Freitas, V.T., Lima, P.P., André, P.S., Ferreira, R.A., Vaz, P.D., Ribeiro-Claro, P., and Carlos, L.D. (2013). Engineering highly efficient Eu (III)-based tri-ureasil hybrids toward luminescent solar concentrators. J. Mater. Chem. A *1*, 7339–7350.

Peng, P., Sadtler, B., Alivisatos, A.P., and Saykally, R.J. (2010). Exciton dynamics in CdS− Ag2S nanorods with tunable composition probed by ultrafast transient absorption spectroscopy. J. Phys. Chem. C *114*, 5879–5885.

Regulacio, M.D., and Han, M.-Y. (2010). Composition-tunable alloyed semiconductor nanocrystals. Acc. Chem. Res. *43*, 621–630.

Ronda, C.R. (2007). Luminescence: From Theory to Applications (John Wiley & Sons).

Sackmann, E.K., Fulton, A.L., and Beebe, D.J. (2014). The present and future role of microfluidics in biomedical research. Nature *507*, 181.

Sadeghi, S., Bahmani Jalali, H., Melikov, R., Ganesh Kumar, B., Mohammadi Aria, M., Ow-Yang, C.W., and Nizamoglu, S. (2018a). Stokes-Shift-Engineered indium phosphide quantum dots for efficient luminescent solar concentrators. ACS Appl. Mater. Interfaces *10*, 12975–12982.

Sadeghi, S., Kumar, B.G., Melikov, R., Aria, M.M., Jalali, H.B., and Nizamoglu, S. (2018b). Quantum dot white LEDs with high luminous efficiency. Optica *5*, 793–802.

Sadeghi, S., Mutcu, S.E., Srivastava, S.B., Aydindogan, G., Caynak, S., Karslı, K., Melikov, R., and Nizamoglu, S. (2018c). High quality quantum dots polymeric films as color converters for smart phone display technology. Mater. Res. Express *6*, 035015.

Sadeghi, S., Abkenar, S.K., Ow-Yang, C.W., and Nizamoglu, S. (2019a). Efficient white LEDs using liquid-state magic-sized CdSe quantum dots. Sci. Rep. *9*, 1–9.

Sadeghi, S., Melikov, R., Bahmani Jalali, H., Karatum, O., Srivastava, S., Conkar, D., Firat Karalar, E.N., and Nizamoglu, S. (2019b). Ecofriendly and efficient luminescent solar concentrators based on fluorescent proteins. ACS Appl. Mater. Interfaces *11* (9), 8710–8716.

Sadeghi, S., Melikov, R., Conkar, D., Firat-Karalar, E.N., and Nizamoglu, S. (2020). Ultra-efficient and high-quality white light-emitting devices using fluorescent proteins in aqueous medium. Adv. Mater. Tech. 2000061. https://doi.org/10.1002/admt.202000061.

Sahu, A., Kang, M.S., Kompch, A., Notthoff, C., Wills, A.W., Deng, D., Winterer, M., Frisbie, C.D., and Norris, D.J. (2012). Electronic impurity doping in CdSe nanocrystals. Nano Lett. *12*, 2587–2594.

Sharma, M., Gungor, K., Yeltik, A., Olutas, M., Guzelturk, B., Kelestemur, Y., Erdem, T., Delikanli, S., McBride, J.R., and Demir, H.V. (2017). Near-unity emitting copper-doped colloidal semiconductor quantum wells for luminescent solar concentrators. Adv. Mater. *29*, 1700821.

Tamang, S., Lincheneau, C., Hermans, Y., Jeong, S., and Reiss, P. (2016). Chemistry of InP nanocrystal syntheses. Chem. Mater. *28*, 2491–2506.

Viswanatha, R., Brovelli, S., Pandey, A., Crooker, S.A., and Klimov, V.I. (2011). Copper-doped inverted core/shell nanocrystals with "permanent" optically active holes. Nano Lett. *11*, 4753–4758.

Wang, B., Liu, H., Zhang, B., Han, Y., Shen, C., Lin, Q., and Chen, H. (2016). Development of antibacterial and high light transmittance bulk materials: incorporation and sustained release of hydrophobic or hydrophilic antibiotics. Colloids Surf. B Biointerfaces *141*, 483–490.

Wang, Z., Yang, W., and Wang, Y. (2017). Self-trapped exciton and large Stokes shift in pristine and carbon-coated silicon carbide quantum dots. J. Phys. Chem. C *121*, 20031–20038.

Wei, M., de Arquer, F.P.G., Walters, G., Yang, Z., Quan, L.N., Kim, Y., Sabatini, R., Quintero-Bermudez, R., Gao, L., and Fan, J.Z. (2019). Ultrafast narrowband exciton routing within layered perovskite nanoplatelets enables low-loss luminescent solar concentrators. Nat. Energy *4*, 197–205.

Won, Y.-H., Cho, O., Kim, T., Chung, D.-Y., Kim, T., Chung, H., Jang, H., Lee, J., Kim, D., and Jang, E. (2019). Highly efficient and stable InP/ZnSe/ZnS quantum dot light-emitting diodes. Nature *575*, 634–638.

Wu, K., Li, H., and Klimov, V.I. (2018). Tandem luminescent solar concentrators based on engineered quantum dots. Nat. Photon. *12*, 105.

Xie, R., and Peng, X. (2009). Synthesis of Cu-doped InP nanocrystals (d-dots) with ZnSe diffusion barrier as efficient and color-tunable NIR emitters. J. Am. Chem. Soc. *131*, 10645–10651.

Xu, S., Ziegler, J., and Nann, T. (2008). Rapid synthesis of highly luminescent InP and InP/ZnS nanocrystals. J. Mater. Chem. *18*, 2653–2656.

Yu, S., Fan, X.-B., Wang, X., Li, J., Zhang, Q., Xia, A., Wei, S., Wu, L.-Z., Zhou, Y., and Patzke, G.R. (2018). Efficient photocatalytic hydrogen evolution with ligand engineered all-inorganic InP and InP/ZnS colloidal quantum dots. Nat. Commun. *9*, 1–10.

Zhao, H., Liang, H., Vidal, F.o., Rosei, F., Vomiero, A., and Ma, D. (2014). Size dependence of temperature-related optical properties of PbS and PbS/CdS core/shell quantum dots. J. Phys. Chem. C *118*, 20585–20593.

Zheng, X., Troughton, J., Gasparini, N., Lin, Y., Wei, M., Hou, Y., Liu, J., Song, K., Chen, Z., and Yang, C. (2019). Quantum dots supply bulk-and surface-passivation agents for efficient and stable perovskite solar cells. Joule *3*, 1963–1976.

Zhou, Y., Zhao, H., Ma, D., and Rosei, F. (2018). Harnessing the properties of colloidal quantum dots in luminescent solar concentrators. Chem. Soc. Rev. *47*, 5866–5890.

iScience, Volume *23*

Supplemental Information

High-Performance, Large-Area, and Ecofriendly Luminescent Solar Concentrators Using Copper-Doped InP Quantum Dots

Sadra Sadeghi, Houman Bahmani Jalali, Shashi Bhushan Srivastava, Rustamzhon Melikov, Isinsu Baylam, Alphan Sennaroglu, and Sedat Nizamoglu

TRANSPARENT METHODS

Chemicals. Indium chloride ($InCl_3$) (99.999%), hexadecylamine (HDA) (98%), zinc undecylenate (98%), stearic acid (SA) (≥98.5%), 1-Octadecene (ODE) (90%), tris(trimethylsilyl)phosphine ($P(TMS)_3$) (95%), copper(II) acetate ($Cu(Ac)_2$) (98%), Zinc stearate ($Zn(St)_2$), selenium (Se) (99.99%) and trioctylphosphine (TOP) (97%) were purchased from Sigma-Aldrich. ODE was purified at 150 °C by evacuation and refilling with nitrogen for 1 h. All the procedures were performed in a nitrogen-filled glovebox with an O_2 level below 0.5 ppm using anhydrous solvents.

$P(TMS)_3$ stock solution. A solution of $P(TMS)_3$ in ODE was prepared with the concentration of 0.2 $mmol.ml^{-1}$ and stored in inert atmosphere at -40 °C.

Copper stearate stock solution. 0.5 mmol $Cu(Ac)_2$ and 1 mmol SA were stirred in 5 ml ODE at 150 °C for 1 h. The solution was kept in inert atmosphere.

Zinc stearate stock solution. 0.1 M solution of zinc stearate in ODE was prepared and stored in inert atmosphere.

Selenium stock solution. 0.1 M solution of selenium in TOP was prepared and stored in inert atmosphere.

Small-scale synthesis of quantum dots. The colloidal synthesis was performed in a nitrogen filled Schlenk line. For InP core synthesis, 0.1 mmol $InCl_3$, 0.2 mmol HDA, 0.1 mmol zinc undecylenate and 0.1 mmol SA were mixed in 3 ml ODE in a three-neck 50 ml round bottom reaction flask. The solution was firstly degassed at 150 °C for 1 h, then heated up to 250 °C under nitrogen atmosphere. 0.5 ml of the $P(TMS)_3$ stock solution was injected to the solution at this temperature. The solution was kept at 230 °C for 20 min and then cooled down to 180 °C. At this temperature, 1 μmol copper stearate was introduced to the solution and then heated up to the 220 °C. For the first ZnSe shelling, 600 μl of the zinc stearate stock solution was added to the reaction flask. After 10 minutes keeping at 220 °C, 600 μl of the selenium stock solution introduced to the reaction. For a successful shelling, the solution was heated up to 280 °C, kept at that temperature for 20 min and finally cooled down to room temperature. For second, third, fourth, fifth and sixth shelling, 825 μl, 1050 μl, 1400 μl, 1750 μl and 2275 μl of stock solution were used, respectively. For purification, ethanol was added to the solutions and then centrifuged at 9000 rpm for 15 min for two times. The precipitated QDs were dispersed in hexane and kept at 5 ºC in inert atmosphere.

Large-scale synthesis of quantum dots. For the large-scale synthesis, the amounts used in the above small-scale section were multiplied by 10. The large-scale synthesis was performed in a 100 ml round-bottom reaction flask. Phosphine solution is extremely air sensitive and needs to be handled very carefully for injection.

Details of the characterization techniques. The transmission electron microscopy (TEM) was performed using a FEI Talos F200S 200 k microscope with an accelerating voltage of 200 keV. For XRD measurements, multiple layers of QD solution were drop-casted on a glass substrate, left to dry, and analyzed in a Bruker D2 Phaser X-ray diffractometer with Cu Kα radiation (λ = 1.541 Å).

Optical properties of quantum dots. The photoluminescence and UV/Visible absorbance spectra of synthesized QDs and the transmission measurement of the fabricated QD-based LSCs were performed by Edinburgh Instruments spectroflourometer FLS1000 with 325 mm focal length monochromator. The excitation source was 450 W ozone free xenon arc lamp that covers a range of 230 nm to >1000 nm for steady state measurements. The QD solutions were excited

with 275 nm and 400 nm wavelengths for PL intensity and PLQY measurements, respectively. The integrating sphere was used to measure absolute PLQY of the synthesized QDs. Standard quartz cuvettes with the cross dimensions of 1 × 1 cm^2 was used for photoluminescence, UV/Visible and PLQY measurements. For the optical properties of the solid-state samples, another sample holder was used. The scatter and emission ranges were adjusted between 370-440 nm and 560-975 nm for the copper-doped samples, respectively. The absolute PLQY measurement method, which was used for the calculation of the PLQY in the FLS1000 integrating sphere module, has an estimated error of ±5%. The repeatability has an error of ±3%. For the calibration of the integrating sphere, Rhodamine 6G dye with the emission peak wavelength of 548 nm and a mean PLQY of 95% was obtained, as expected. The number of recorded signal photons (i.e., detector linearity) was adjusted as 1 million photons per second to eliminate the instrumental factors affecting the measured PLQY of the QDs. Time-resolved spectroscopy was carried out by Picoquant MicroTime 100 time-resolved confocal fluorescence microscope. The excitation beam was provided by an 8 mW picosecond diode laser (λ_{ex} = 375 nm) pulsed at 250 KHz repetition rate to 40X objective lens. A single photon sensitive detector (PMA Hybrid 50) based on a photomultiplier tube (R10467 from Hamamatsu) was used. The time-correlated single photon counting electronics of HydraHarp 400 was adjusted to a resolution of 4 ps. All of the time-resolved measurements were performed on QD solutions with the optical density of approximately 0.1 at the first excitonic peak at room temperature.

Accelerated-ageing test. In the accelerated-ageing test, firstly the acceleration factor was calculated by considering the absorbance of the QDs inside the film (0.35) at the illumination wavelength (365 nm). This absorbance value is corresponding to 55.3% absorbance. The absorbance of the film (55.3%) was multiplied with the calculated power density of the UV lamp at 365 nm (~8 $mW.cm^{-2}$) and resulted in 4.43 $mW.cm^{-2}$ of the absorbed power at the excitation wavelength. By dividing the value of absorbed power with the ratio of the absorbed photons by the film under 1 sun condition (~6%), the acceleration factor of ~74 was achieved. The quantum efficiency measurement of the QD film was performed under 16 hours and multiplied to the acceleration factor, which result in ~50 days.

Femtosecond pump-probe spectroscopy. The non-linear absorption properties and ultrafast decay dynamics of the QDs were investigated by using a femtosecond pump-probe spectrometer (Helios, Ultrafast Systems). The QD solution was excited at 400 nm by using the fourth-harmonic output of a tunable, femtosecond optical parametric amplifier (OPA, TOPAS Prime, Spectra-Physics), which was pumped with a 2-mJ, 800-nm Ti^{3+}: sapphire regenerative amplifier (pulse duration: 120 fs, pulse repetition rate: 1 kHz, Spitfire Ace, Spectra-Physics). A portion of the 800-nm output of the regenerative amplifier was further focused inside a sapphire plate to generate the femtosecond white light continuum probe pulses in the 450-800 nm wavelength range (see **Fig S16**). The white light continuum probe was split into two before passing through the sample. One of them was directly sent to the sample and the other beam was used as a reference to monitor the fluctuations in the generated white light continuum intensity during the measurements. In the pump-probe spectroscopy experiments, the pump and probe beams were overlapped and focused inside a 0.5-mm-long spectrosil cuvette containing QD solution with the optical density of 1 at the band-edge absorption. The average number of electron-hole pairs ($N_{e\text{-}h}$) generated during the pumping process was calculated from $N_{e\text{-}h}=J/J_{sat}$, where J is the photon fluence and the saturation fluence J_{sat} is given by $h\nu_{pump}/\sigma_a$ (Sennaroglu et al., 2006). During the pump-probe experiments, the 400-nm fluence (J) incident on the QDs was sufficiently low (135 $\mu J/cm^2$), giving $N_{e\text{-}h}=0.5$.

The fabrication of the QD-based LSC. The synthesized QD solutions dissolved in hexane were mixed with the silicon elastomer (SYLGARD 184) and curing agent with the

concentrations of 13 mg.ml^{-1}, 26 mg.ml^{-1} and 52 mg.ml^{-1}. The ratio of the curing agent to the elastomer was adjusted to 1/10. Then, the mixture was stirred for 5-10 minutes until the bubbles appeared. The mixture was degassed at the vacuum desiccator for 1 hour to remove the bubbles and form a homogenous mixture. After the degassing process, the QD-polymer composite was poured on the glass substrate with different dimensions to form a strip in front of the doctor-blade device. The doctor-blade was translated over the LSC length to from a thin QD-polymer composite layer. The substrate was cured at the oven at 70 °C to remove hexane solvent and form a high-quality film. The thickness of the glass substrate in all QD-LSC structures was 2 mm. The curing of the large-area QD-based LSC after the deposition of the QD-polymer mixture was performed over the hot plates.

The optical properties of QD-LSC. For reabsorption measurement, a picosecond pulsed diode laser (EPL) from Edinburgh Instruments with operation wavelength of 365 nm and pulse width of 65 ps, repetition rate of 20 MHz, average output power of 5 mW and horizontal polarization was used for the excitation of the QD-LSCs at different optical distances. For scattering measurements, a continuous-wave Ti:sapphire laser operating at 780 nm with the power of 900 mW and horizontal polarization was used.

Electro-optical measurements. For electro-optical measurement, a calibrated Newport Oriel LCS-100 solar simulator AM 1.5G was used according to the ref (Yang et al., 2019). The output power of the Xe lamp was 100 mW.cm^{-2}. Two different silicon solar cells with dimensions of 11 × 7 cm^2 and 24 × 24 cm^2 were used for the efficiency measurements of QD-LSCs with different dimensions. Since the surface area of solar cells were greater than LSC edge area, a black tape was used to mask the excessive area. During the measurement, the uncoupled edges of the LSCs were covered with black paint and only one edge was coupled to the solar cell in order to eliminate any incident light from outside and PL reflection back to the waveguide. Depending on the size of the fabricated QD-LSCs, a mate black paper was placed at the back of the LSC in order to block any direct illumination from the solar simulator.

The simulation of the optical and external quantum efficiency of QD-based LSCs. The optical quantum efficiency of the LSC (Equation (S1) (Wu et al., 2018) is directly proportional with QE of the QDs embedded inside the polymeric matrix (η_{PL}) and light trapping efficiency inside the waveguide (η_{TIR}). η_{PL} is already measured in an integrating sphere (Fig. 3d of the manuscript) and it is 81.2%. $\eta_{TIR} = \cos(\arcsin 1/n)$ (Klimov et al., 2016) is 74.5% for glass with a refractive index (n) of 1.51 in the visible wavelength region. By using the measured scattering (s_2) and absorption coefficient (α_{2eff}) of the LSC (based on Fig. S8 and S9), the calculated optical quantum efficiency corresponded to 49.9% for LSC with the loading concentration of 26 mg.ml^{-1} and side length of 10 cm. The optical quantum efficiency values of the QD-LSC with the side length of 10 cm at the loading concentrations of 13 and 52 mg.ml^{-1} were also corresponding to 51.8% and 46.7%, respectively (Fig. 6c). Moreover, by changing the side length to 5 and 20 cm, the optical quantum efficiency of LSC with the loading concentration of 26 mg.ml^{-1} corresponded to 54.8% and 42.7%, respectively (Fig. 6d).

$$\eta_{OQE} = \frac{\int \frac{\eta_{TIR}\eta_{PL}}{1+\beta(\alpha_{2eff}+s_2)L\left(1-\left(\frac{\alpha_{2eff}\eta_{PL}+s_2}{\alpha_{2eff}+s_2}\right)\eta_{TIR}\right)} \phi_{PL}(\lambda)d\lambda}{\int \phi_{PL}(\lambda)\mathrm{d}\lambda} \quad \text{(S1)}$$

Absorption efficiency, which quantifies the number of the absorbed photons over solar spectrum was calculated based on Equation (S2) (Klimov et al., 2016) as follows:

$$\eta_{abs} = \frac{\int \phi_{sol}(1-\mathrm{R})\left(1-e^{-\alpha(\lambda)d}\right)d\lambda}{\int \phi_{sol}(\lambda)\mathrm{d}\lambda} \quad \text{(S2)}$$

$\phi_{sol}(\lambda)$ is the spectral profile of the solar spectrum (Fig. S10). R is reflectivity, which was calculated based on Equation (S3). d was considered as the LSC thickness and α(λ) is the absorption coefficient of the copper-doped InP/5 ML ZnSe QDs calculated from absorbance spectrum (Fig. S7b).

$$R = \frac{(n_2 - n_1)^2}{(n_2 + n_1)^2} \qquad \text{(S3)}$$

The simulated values of external quantum efficiency was calculated based on Equation (S4).

$$\eta_{EQE} = \eta_{OQE}\eta_{abs} \qquad \text{(S4)}$$

The external quantum efficiency of the LSCs with different side lengths and loading concentration of the QDs was shown in Fig. S11 and Table S3.

Reshaping factor (q_{LSC}). q_{LSC} is the reshaping factor, which was calculated based on Equation (S5) (Wu et al., 2018).

$$q_{LSC} = \frac{<Q_{PL}>}{<Q_s>} = \frac{\int \phi_{PL}(\lambda)\mathrm{EQE}(\lambda)\mathrm{d}\lambda}{\int \phi_{sol}(\lambda)\mathrm{EQE}(\lambda)\mathrm{d}\lambda} \qquad \text{(S5)}$$

In Equation (S5), $\phi_{PL}(\lambda)$, EQE(λ), and $\phi_{sol}(\lambda)$ are the photoluminescence spectral profile of the copper-doped QDs (Fig. 3a of the manuscript), external quantum efficiency of the silicon solar cell and the spectral profile of the solar spectrum that obtained from the solar simulator (Fig. S10), respectively. Based on Equation (S5), $<Q_{PL}>$ and $<Q_s>$ were calculated as 0.9098 and 0.5253, respectively, which resulted in the q_{LSC} as 1.73. In order to compare the calculated reshaping factor in this study with the previous studies, we used the similar integration method and wavelength range and calculated the reshaping factor of the standard PV cell. Our calculations also resulted with the reshaping factor of 2 for a standard PV cell similar to previous study (Li et al., 2016).

Calculation of coupling efficiency ($\eta_{coupling}$). As mentioned in the main text, in the electro-optical measurements, the solar cells were attached to the LSC edges in order to absorb the incoming photons. In the experimental setup, no refractive-index-matching adhesive was used between LSCs and solar cells. As a result, there will be a photon-loss due to the thin air gap between the LSC edge and coupled solar cells. Based on the refractive index difference between the LSC, air and the solar cell, we calculated the ratio of the number of photons reaching into the cell with respect to the number of photons reaching to the LSC edge. We introduced it as the coupling efficiency ($\eta_{coupling}$). For the calculation of the coupling efficiency, Fresnel equations (Equations (S6) and (S7)) were used as follows (Weber and Lambe, 1976):

$$R_s = \left| \frac{n_1 \cos(\theta_i) - n_2 \sqrt{1 - (\frac{n_1}{n_2}\sin(\theta_i))^2}}{n_1 \cos(\theta_i) + n_2 \sqrt{1 - (\frac{n_1}{n_2}\sin(\theta_i))^2}} \right|^2 \qquad \text{(S6)}$$

$$R_p = \left| \frac{n_2 \cos(\theta_i) - n_1 \sqrt{1 - (\frac{n_1}{n_2}\sin(\theta_i))^2}}{n_2 \cos(\theta_i) + n_1 \sqrt{1 - (\frac{n_1}{n_2}\sin(\theta_i))^2}} \right|^2 \qquad \text{(S7)}$$

$$R_{eff} = \frac{R_s + R_p}{2} \qquad \text{(S8)}$$

Photoluminescence of QDs is unpolarized. Hence, effective reflectance can be calculated by averaging s and p polarization equations (see Equation (S8)). Generated light travels from glass to air (R_{s1}, R_{p1}) and then from air to solar cell (R_{s1}, R_{p1}), hence the coupling efficiency can be calculated based on Equation (S9) as follows:

$$\eta_{coupling} = \sum_0^{90-\theta_c} \left(1 - R_{eff1}(\theta)\right)\left(1 - R_{eff2}(\theta)\right)/(90 - \theta_c) \quad \text{(S9)}$$

It should be noted that only guided light can reach to edge of the luminescent solar concentrator, hence reflectance are averaged from 0 to 90 – θ_c, all other light confined in the luminescent solar concentrator. Here, θ_c = 41.5° and s and p polarization reflectance were shown in Fig. S12 and S13. Using Equation (S8), effective reflectance of un-polarized PL from glass to air under solar cell is 4.39% when integrated from 0° to 48.5°. Similarly, when the light moves from air to solar cell, effective reflectance is 21.26%. Using Equation (S9), the coupling efficiency was yielded as $\eta_{coupling} = 75.2\%$.

Optical quantum efficiency measurements. The measurement results extracted from Fig. 6a of the manuscript and Fig. S15 were shown in Table S4. As also mentioned in the manuscript, in order to measure the optical quantum efficiency values for the fabricated devices, Equation (S10) was used as follows (Wei et al., 2019):

$$\eta_{OQE}\ (\%) = \frac{J_{LSC}}{J_{PV} \times G \times q_{LSC} \times \eta_{abs} \times \eta_{coupling}} \quad \text{(S10)}$$

For the measurement of optical quantum efficiency, it should be mentioned that the short circuit current values represent the number of photons reached to the solar cells. However, the optical quantum efficiency considers the number of photons exiting from the LSC edge. As a result, the values obtained from the electro-optical measurements need to be divided by the coupling efficiency in order to obtain the optical quantum efficiency values for different QD-LSCs.

The optical gain factor (G-factor). The optical gain factor was measured based on G = L / (4D), in which the L is the side length of LSC and D is the thickness of the QD-LSC equal to approximately 0.2 cm. As a result, the G factor for the devices with the LSC lengths of 5, 10 and 20 cm yielded to 6.25, 12.5 and 25, respectively.

The power conversion efficiency (PCE) measurements. The power conversion efficiency of the QD-LSCs were calculated by using Equation (S11) (Wu et al., 2018).

$$\text{PCE}\ (\%) = \eta_{EQE-LSC}\eta_{EQE-PV} \quad \text{(S11)}$$

, in which the $\eta_{EQE\text{-}LSC}$ is the measured external quantum efficiency of the device based on the electro-optical measurements (Table S4) and $\eta_{EQE\text{-}PV}$ is the external quantum efficiency of the PV cells equal to 14.5% based on Fig. S14.

The comparison between the external quantum efficiency of this study and previous studies. Based on Table S5, the measured optical quantum efficiency of the fabricated QD-LSCs with the dimensions of 10 cm × 10 cm under the illumination of AM 1.5G solar simulator in this study is comparable with the highest values reported in the literature.

In reference (Wei et al., 2019), the authors reported the optical quantum efficiency level of 26% with the same dimensions of this study and higher thickness of the film (0.2 cm).

In reference (Meinardi et al., 2017), for the calculation of the optical quantum efficiency, the reshaping factor has not been considered in the calculations, which may lower the reported value of 30%. We used the emission profile of the QDs in reference (Meinardi et al., 2017) in order to calculate the reshaping factor (PL wavelength range from 560-1040 nm centered at 830 nm). Our calculations yielded to the values of 0.9126 and 0.4592 for $\langle Q_{PL} \rangle$ and $\langle Q_s \rangle$, respectively. As a result, the q_{LSC} was calculated as 1.9874. By dividing the reported value of η_{OQE} (~30%) by the calculated reshaping factor (~2), the η_{OQE} was decreased nearly two-fold to a new value of 15%, almost half of the reported value in this study (28%). The significant

deference in the optical quantum efficiencies is due to the difference in the QE of the QDs, which was almost two times higher in this study (81.2%) in comparison with the reported value for silicon QDs (46%) in the previous study.

The calculation of the visible light transmittance (VLT). Equation (S12) was used in order to calculate the weighted average visible light transmittance (VLT) of the LSC windows according to reference (Bergren et al., 2018) as follows:

$$\text{visible light trasmittance (VLT)} = \frac{\int T(\lambda)P(\lambda)S(\lambda)d\lambda}{\int P(\lambda)S(\lambda)d\lambda} \quad \text{(S12)}$$

, where T (λ) is the transmittance of the window, P (λ) is the eye-sensitivity function and S (λ) is the solar spectrum. The wavelength range was adjusted to 300-750 nm (i.e., visible wavelength region). Our calculations showed that the fabricated QD-LSCs with the loading concentration of 52 mg.ml^{-1} has the VLT value of 41%. As a result, the VLT of the fabricated LSCs with lower concentration will be >41%, which can be used as tinted architectural windows.

The consistency check for the calculation of external quantum efficiency values. As the final consistency check for the calculated values of the EQE of the LSC devices, we used the formulation in the recent study (Yang et al., 2019). In the reference, the authors used Equation (S13) for the calculation of the external quantum efficiency of the LSC as follows:

$$\eta_{LSC} = \eta^*_{opt}\eta^*_{PV} \quad \text{(S13)}$$

, in which η^*_{opt} and η^*_{PV} was calculated based on Equations (S14) and (S16), respectively.

$$\eta^*_{opt} = \frac{\int \text{AM 1.5G}\,(\lambda)\,\eta_{opt}(\lambda)d\lambda}{\int \text{AM 1.5G}\,(\lambda)d\lambda} \quad \text{(S14)}$$

In Equation (S14), $\eta_{opt}(\lambda)$ is the optical efficiency of the LSC at different wavelengths. For the calculation of the optical efficiency, Equation (S15) was used.

$$\eta_{opt} = \left(1 - R_f(\lambda)\right) A(\lambda)\,\eta_{PL}\eta_{TIR}\eta_{wg} \quad \text{(S15)}$$

In Equation (S15), R_f (λ) is the reflection spectrum of the incident light at the front surface. A(λ) is the absolute absorption spectrum, η_{PL} is the quantum efficiency of the QDs in-film as 81.2%, η_{TIR} and η_{wg} are 74.5% and 73.6% based on the calculations in the main text, respectively. As a result, η^*_{opt} yielded to 35.2%. η^*_{PV} was calculated based on Equation (S16) as follows:

$$\eta^*_{PV} = \left[\frac{\eta_{PV}\,(AM\ 1.5G)}{\eta^{PV}_{abs}(AM\ 1.5G)}\right]\frac{\int \text{EQE}_{PV}\,(\lambda')\,PL(\lambda')d\lambda'}{\int PL(\lambda')d\lambda'} \quad \text{(S16)}$$

In Equation (S16), $\eta_{PV}(AM\ 1.5G)$ is the power conversion efficiency of the edge-mounted PV cell under the AM 1.5G solar illumination, $PL(\lambda')$ is the emission profile of the synthesized QDs in the device architecture, and $\eta^{PV}_{abs}(AM\ 1.5G)$ is the absorption efficiency of the silicon photovoltaics. Based on our calculations, η^*_{PV} corresponded to 16.2%. As a result, the external quantum efficiency η_{LSC} of the LSC corresponded to 5.7%, which is in close approximation of our measured external quantum efficiency based on the electro-optical measurements (5.9% as shown in Table S4).

Supplemental Figures and Tables

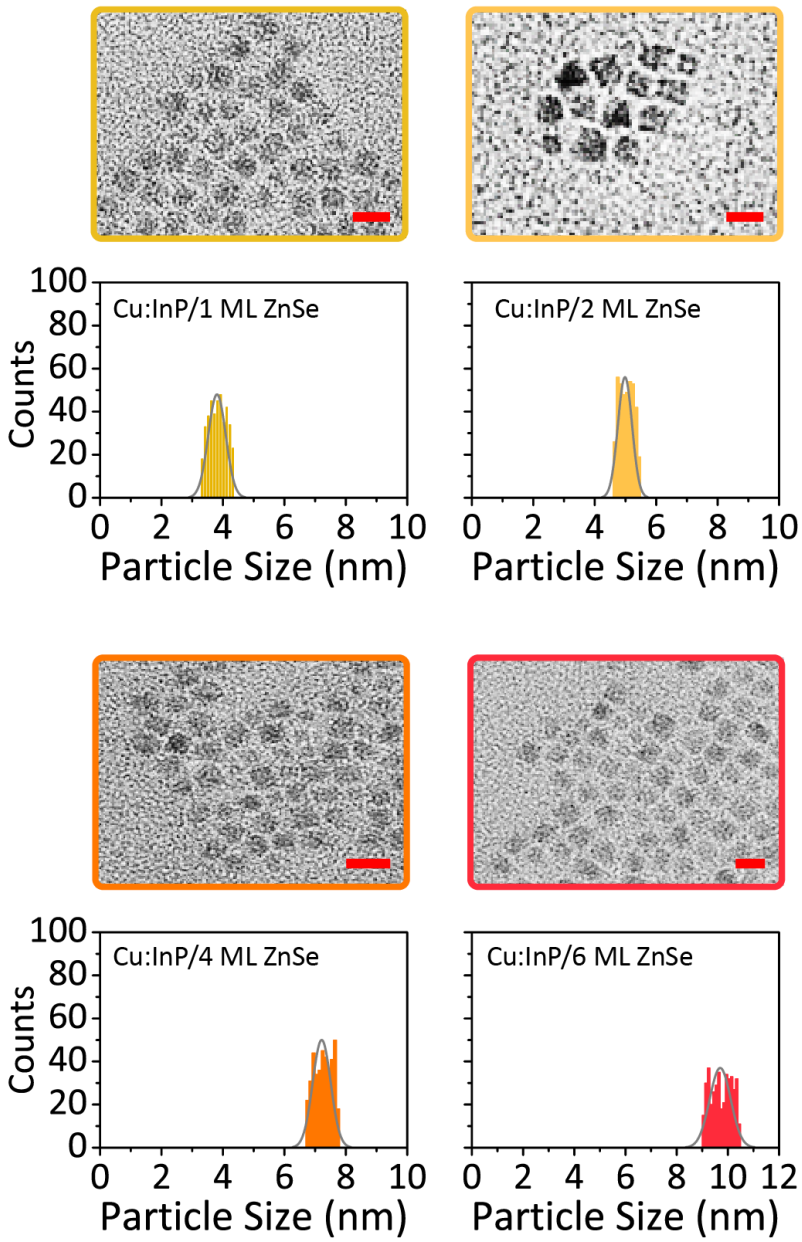

Figure S1. Related to Figure 2. The TEM images and size distribution of copper-doped InP QDs with 1, 2, 4 and 6 ML of ZnSe shell. The scale bar in two upper panel images = 5 nm and in two lower panel images = 10 nm.

Table S1. The mean size of the synthesized QDs in each step of the synthesis procedure. Related to Figure 2.

Type	InP	Cu:InP	1 ML ZnSe	2 ML ZnSe	3 ML ZnSe	4 ML ZnSe	5 ML ZnSe	6 ML ZnSe
Size (nm)	2.5 ± 0.2	2.7 ± 0.2	3.8 ± 0.3	5.0 ± 0.3	6.3 ± 0.2	7.2 ± 0.3	8.5 ± 0.3	9.7 ± 0.4

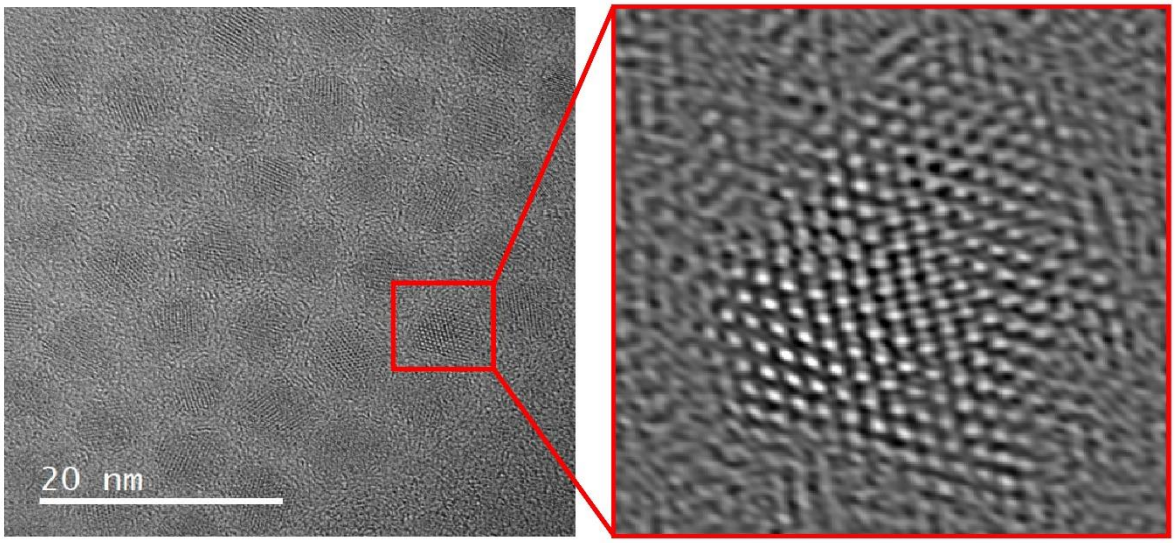

Figure S2. Related to Figure 2. The high-resolution TEM (HRTEM) image of the synthesized copper-doped InP/5ML ZnSe QDs.

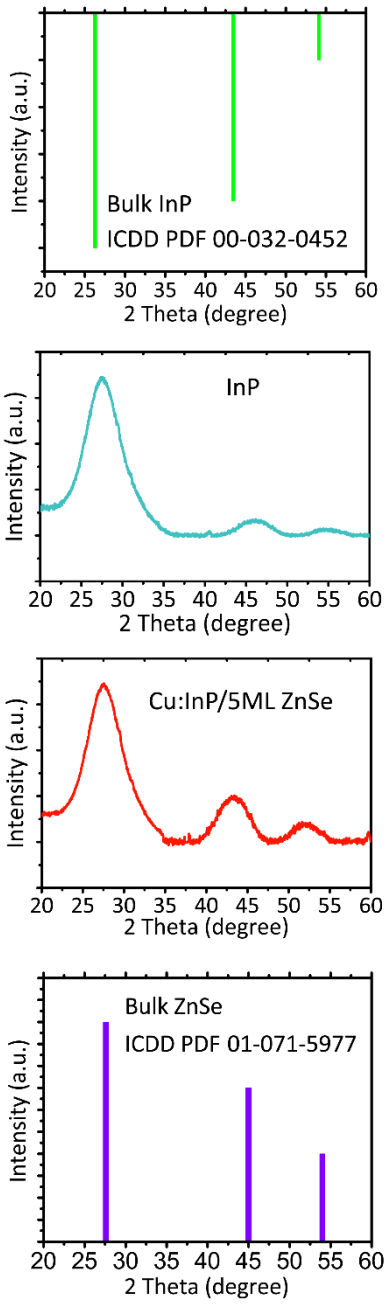

Figure S3. Related to Figure 2. The XRD patterns of InP and copper-doped InP/5ML ZnSe QDs. The top and bottom panels show the XRD peaks of the bulk InP and ZnSe, respectively.

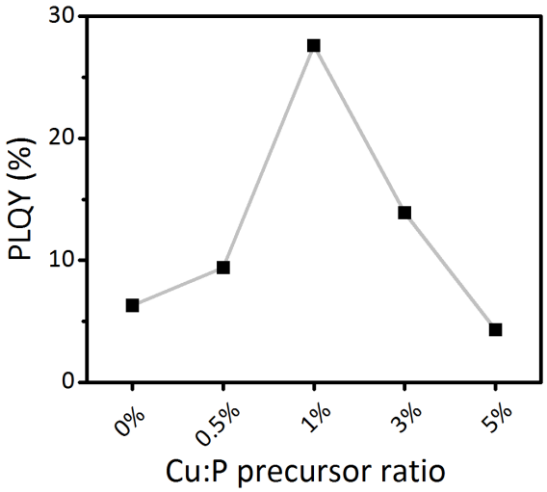

Figure S4. Related to Figure 3. The evolution of the PLQY by increasing Cu:P precursor ratio. At the Cu:P ratio of 1%, the highest PLQY of 27.6% was achieved.

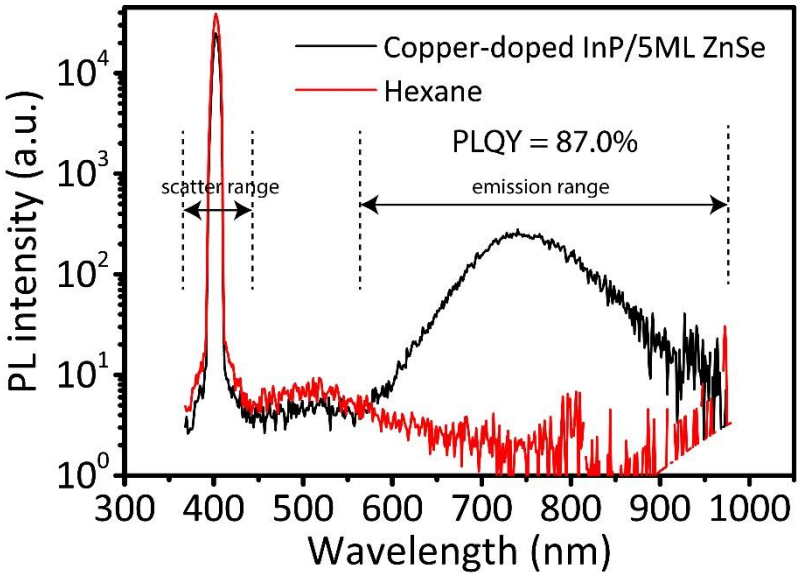

Figure S5. Related to Figure 3. The PL intensity spectra of the synthesized copper-doped InP/5ML ZnSe QDs and hexane solvent as the reference for the PLQY measurement.

Table S2. The comparison between the PLQY of the QDs in this study and the previous studies synthesized in the near infrared wavelength region. Related to Figure 3.

	Type of the QDs	Photoluminescence peak wavelength range (nm)	FWHM (nm)	PLQY (%)	Stokes-shift (meV)	Ref
1	Copper-doped CdSe	650-700	~115	97	~1400	(Sharma et al., 2017)
2	Ag-doped InP	900	~250	40	~520	(Vinokurov et al., 2018)
3	InAs/InP/ZnSe	940	60-75	76	~140	(Xie et al., 2008)
4	GSH-coated PbS	950-1200	~250	16	---	(Nakane et al., 2013)
5	PbS	900-1050	250	17	~120	(Bakueva et al., 2004)
6	Ag_2Te/ZnS	1000-1100	200	5.6	---	(Chen et al., 2013)
7	PEGylated-DHLA-Ag_2S	1150-1220	43	15.5	---	(Zhang et al., 2012)
8	$CuInS_2$/ZnS	862	250	91	550	(Bergren et al., 2018)
9	$CuInSe_2$/ZnS	805	150	72	160	(Wu et al., 2018)
10	Manganese-doped $Cd_xZn_{1-x}S$/ZnS	600	200	78	750	(Wu et al., 2018)
11	Copper-doped InP	630-1100	100-175	23	~1630	(Xie and Peng, 2009)
12	$CuInS_2$/CdS	750	150	75	500	(Sumner et al., 2017)
13	$CuInSe_xS_{2-x}$/ZnS	965	260	40	530	(Meinardi et al., 2015)
14	Si	830	240	50	400	(Meinardi et al., 2017)
15	CdSe/CdS/CdZnS/ZnS	630	100	45	~50	(Bomm et al., 2011)
16	CdSe/$Cd_{1-x}Zn_xS$	628	60	70	720	(Li et al., 2016)
17	CdSe/$Cd_xPb_{1-x}S$	560-620	23-26	40	300	(Zhao et al., 2016)
18	PbS/CdS	850-1550	---	40-50	250	(Zhou et al., 2016)
19	CdSe/CdS	640	65	45	400	(Meinardi et al., 2014)
20	Copper-doped InP/5ML ZnSe (This study)	720-775	165	87	650	---

Figure S6. Related to Figure 6. The fabricated large-area QD-based LSCs. (a) The large-area QD-LSC with the dimensions of 100 cm× 30 cm under ambient light. **(b)** The zoomed view of the scale for better visualization.

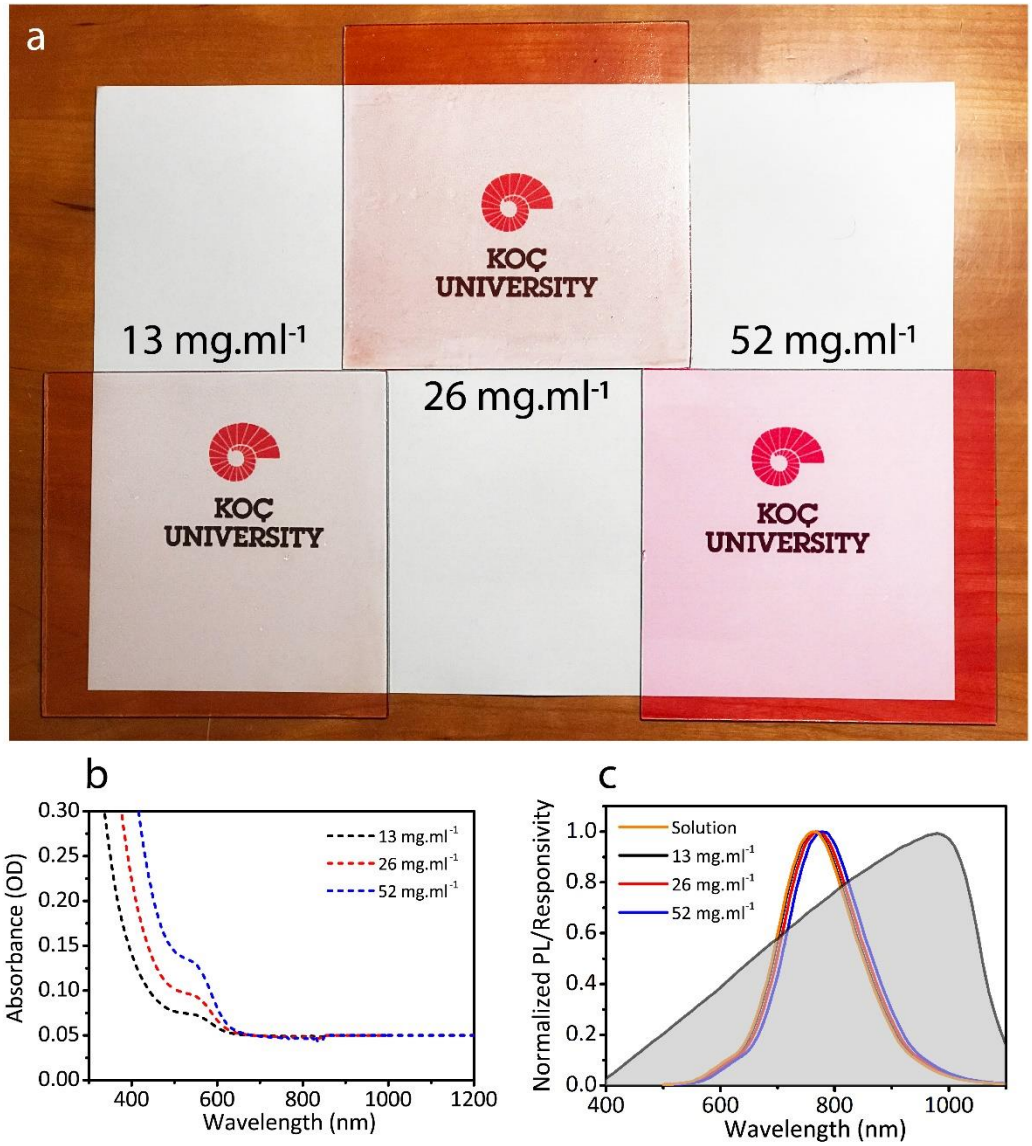

Figure S7. Related to Figure 5. QD-based LSCs with different loading concentrations of copper-doped InP/5 ML ZnSe QDs. (a) The photograph, (**b)** the absorbance and **(c)** the normalized PL output of the fabricated QD-based LSCs with different QD loading concentrations of 13, 26, and 52 mg.ml^{-1}. The grey shaded spectrum in (c) is the responsivity of silicon PV.

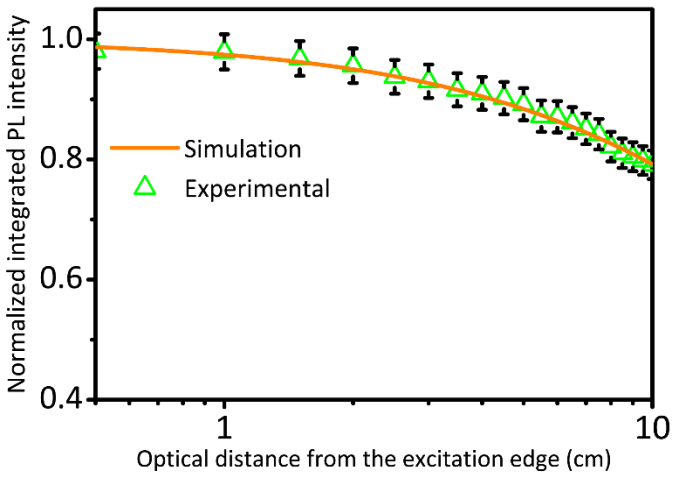

Figure S8. Related to Figure 5. The optical output decay in the fabricated QD-LSC. The spectrally integrated output of QD-based LSC under the illumination by an ultraviolet laser beam at 365 nm wavelength. Orange line shows the simulation results. The reabsorption coefficient was done by the calculation of α in the fitted waveguiding efficiency by using the equation of $\eta_{\text{waveguiding}} = 1/(1+\beta(\alpha_{2,\text{eff}}+s_2)\text{L}[1-((\alpha_{2eff}\eta_{PL}+s_2)/(\alpha_2 eff+s_2))\eta_{TIR}]$. The QD concentration is 26 mg.ml^{-1}.

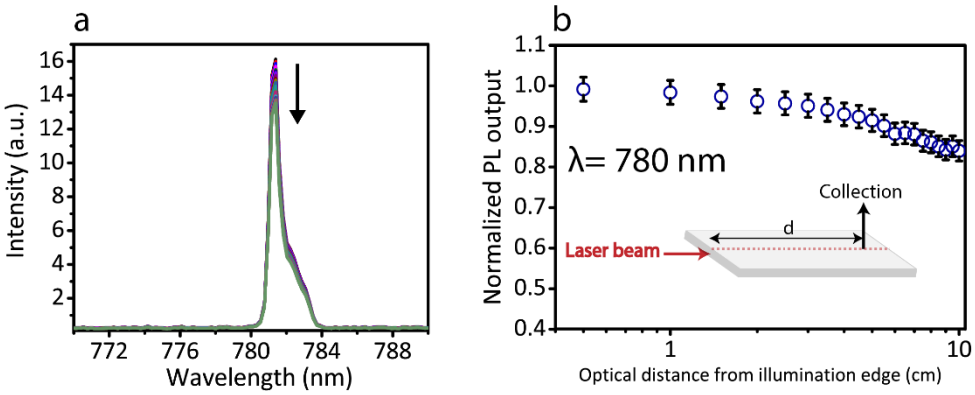

Figure S9. Related to Figure 5. The scattering measurements of the fabricated QD-based LSC. (a) The PL output was shown at different optical distances ranging from 0 to 10 cm in the arrow direction when the laser beam with the wavelength of 780 nm was propagated inside the slab based on the setup schematic demonstrated at (b)-inset. **(b)** The normalized PL output was shown at different optical distances ranging from 0 to 10 cm when the laser beam with the wavelength of 780 nm was propagated inside the slab. Inset: The schematic demonstrates the setup, in which the QD-based LSC illuminated by the laser beam at the edge and the optical output was collected from the face by using an optical fiber.

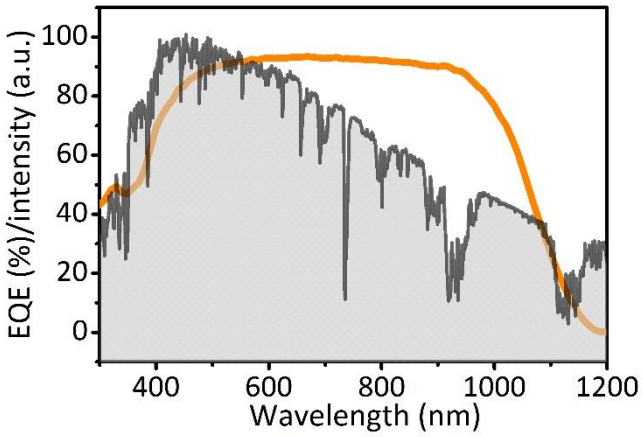

Figure S10. Related to Figure 6. The EQE of the silicon solar cell and the intensity profile of the solar simulator. The orange line shows the EQE graph of the silicon solar cell and the grey shaded area shows the intensity profile of the solar simulator used in this study.

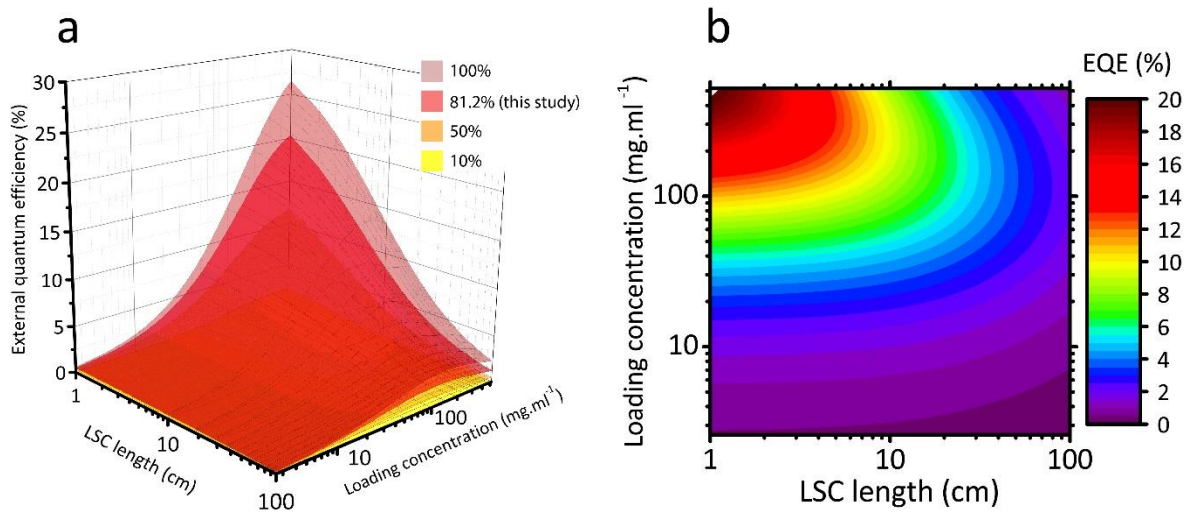

Figure S11. Related to Figure 6. The calculated external quantum efficiency values for the QD-LSC (a) The simulation of the external quantum efficiency of QD-LSCs having different QE of QDs ranging from 10%, 50%, 81.2% (QE of this study) and unity at different LSC lengths ranging from 1 to 100 cm and different loading concentration between 2.6 and 520 mg.ml^{-1}. **(b)** The contour plot of the external quantum efficiency of the QD-LSC having QE of QDs of 81.2%.

Table S3. The summary of the calculation results for the fabricated LSCs with different loading concentrations and side lengths. Related to Figure 6.

Device number	Side length (cm)	Loading concentration (mg.ml^{-1})	Absorption efficiency (η_{abs})	Optical quantum efficiency (η_{OQE})	External quantum efficiency (η_{EQE})
1	5	26	6.9%	54.8%	3.8%
2	10	13	3.6%	51.8%	1.9%
3	10	26	6.9%	49.9%	3.5%
4	10	52	12.1%	46.7%	5.7%
5	20	26	6.9%	42.7%	3.0%

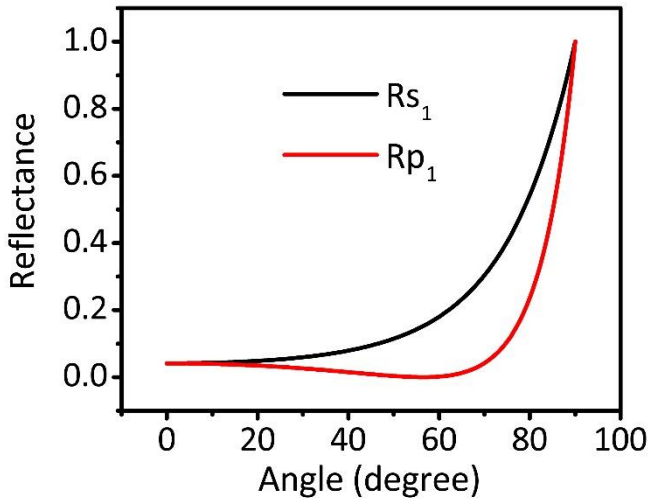

Figure S12. Related to Figure 6. s and p polarization reflectance values from air to PV.

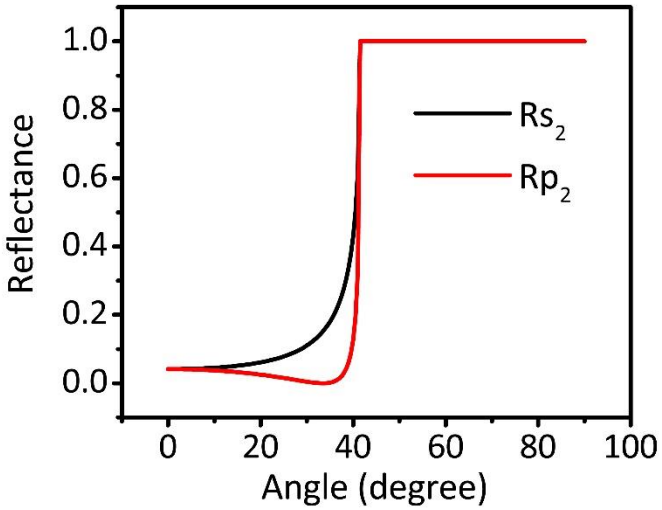

Figure S13. Related to Figure 6. s and p polarization reflectance values from glass to air.

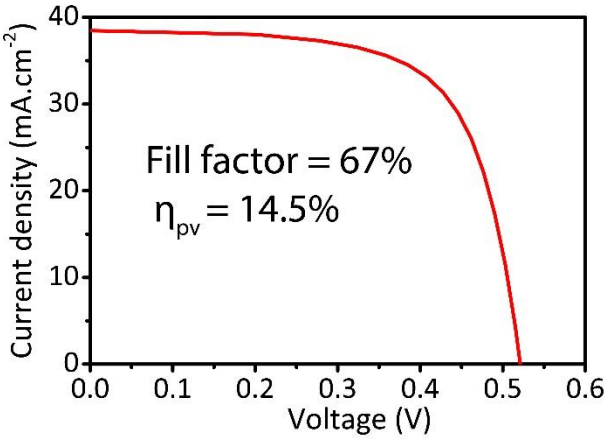

Figure S14. Related to Figure 6. The J-V curve of the silicon solar cell used for the electro-optical measurements under the solar illumination with the power of 100 mW.cm^{-2}.

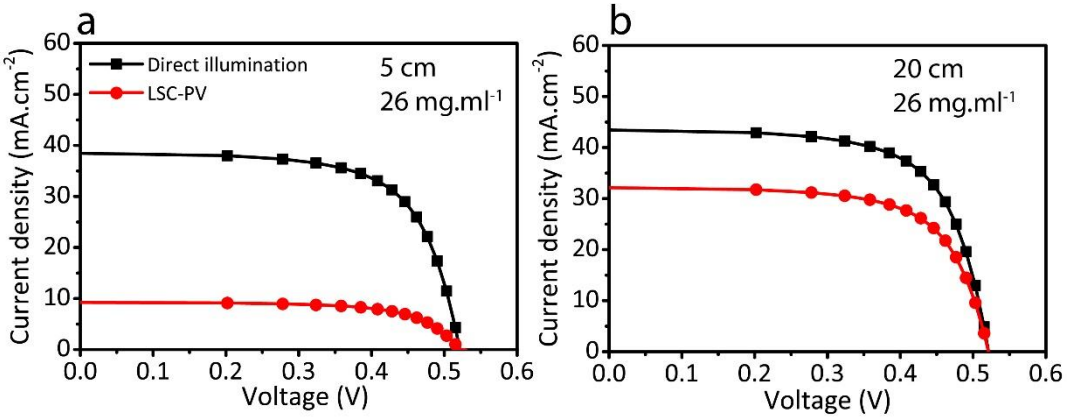

Figure S15. Related to Figure 6. The electro-optical measurement results. The J-V curves of the silicon solar cells coupled to the QD-LSCs with the loading concentration of 26 mg.ml^{-1} and the LSC length of **(a)** 5 cm and **(b)** 20 cm.

Table S4. The summary of the electro-optical measurement results for the fabricated LSCs with different loading concentrations and side lengths. Related to Figure 6.

Device number	Side length (cm)	Loading concentration (mg.ml^{-1})	Geometrical factor (G)	J_{LSC}/J_{PV}	EQE	Optical quantum efficiency	External optical efficiency (EQE/q_{LSC})	PCE
1	5	26	6.25	0.24	3.9%	44.3%	2.3%	0.6%
2	10	13	12.5	0.24	1.9%	40.7%	1.1%	0.3%
3	10	26	12.5	0.44	3.5%	39.9%	2.0%	0.5%
4	10	52	12.5	0.74	5.9%	37.2%	3.4%	0.9%
5	20	26	25	0.73	2.9%	32.7%	1.7%	0.4%

Table S5. The comparison between this study and the previous studies in the literature. Related to Figure 6.

Fluorophore		Type	LSC active area (cm×cm)	Light source	η_{OQE} (%)	EQE (%)	Ref
	1	$CdSe/Cd_{1-x}Zn_xS$	10.2 × 10.2	405 nm light solar simulator	24 21	1.9	(Li et al., 2016)
	2	CdSe/CdS	21.5 × 1.35	solar simulator	10	0.6	(Meinardi et al., 2014)
	3	$(PEA)_2MAPb_2Br_7$ Layered perovskite	10 × 10	solar simulator	26	0.9	(Wei et al., 2019)
	4	$CsPb(I_xBr_{1-x})_3$	1.3 × 9	solar simulator	5	2	(Zhao et al., 2017)
	5	Si	12 × 12	solar simulator	30	---	(Meinardi et al., 2017)
	6	Carbon dots	1.5 × 9	solar simulator	2.6	0.2	(Zhou et al., 2018)
	7	$CuInS_2/ZnS$	10 × 10	solar simulator	23	8.1	(Bergren et al., 2018)
	8	$CuInSe_xS_{2-x}/ZnS$	12 × 12	solar simulator	17	3.3	(Meinardi et al., 2015)
	9	$CuInS_2$	30 × 30	Solar simulator	29.2	6.8	(Anand et al., 2019)
	10	Copper-doped InP/ZnSe (This study)	10 × 10	solar simulator	37.2	5.9	---
	11	Manganese-doped $Cd_xZn_{1-x}S/ZnS$	12 × 12	385 nm light	58	3.4	(Wu et al., 2018)
	12	$CuInSe_2/ZnS$	12 × 12	385 nm light	19	5.1	(Wu et al., 2018)
	13	Manganese-doped ZnSe	2.5 × 7.5	400 nm light	37	---	(Erickson et al., 2014)
	14	CdSe/CdS	2 × 2	400 nm light	59	---	(Coropceanu and Bawendi, 2014)
	15	Copper-doped CdSe	10 × 10	---	---	1.65	(Sharma et al., 2017)
	16	Tandem structure from No. (1) and (2)	15.2 × 15.2	---	---	6.4	(Wu et al., 2018)

	17	$CuInS_2/CdS$	7.5 × 7.5	---	---	5.7	(Sumner et al., 2017)
	18	CdSe/CdS/CdZnS/ZnS	4.95 × 3.1	---	---	---	(Bomm et al., 2011)
	19	$CdSe/Cd_xPb_{1-x}S$	7 × 1.5	---	---	1.4	(Zhao et al., 2016)
	20	PbS/CdS	2 × 1.5	---	---	6.1	(Zhou et al., 2016)
	21	InP/ZnO	9 × 1.5	---	---	3.22	(Sadeghi et al., 2018)
	22	Carbon dots- tandem	10 × 10	---	---	1.1	(Zhou et al., 2018)
Organic Dyes	23	Lumogen F Red305 Fluorescence Yellow CRS 040	5 × 5	---	---	---	(Slooff et al., 2008)
	24	DCJTB	3 cm^2	---	---	3.84	(Zhou et al., 2015)
	25	Pyrromethene 567	10 × 10	---	---	---	(Tummeltshammer et al., 2016)
	26	TPFE-Rho	1.8 × 1.8	---	---	3.55	(Ma et al., 2019)
Fluorescent proteins	27	mScarlet fluorescent protein	1.5 × 1.5	---	---	4.42	(Sadeghi et al., 2019)

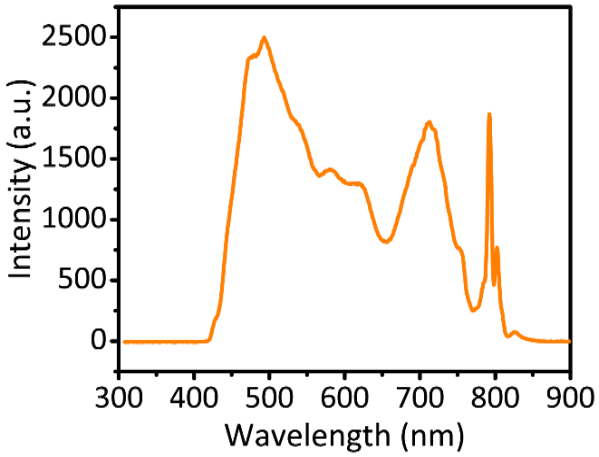

Figure S16. Related to Figure 4. The measured white light continuum spectrum, which was used as the probe beam during the experiments.

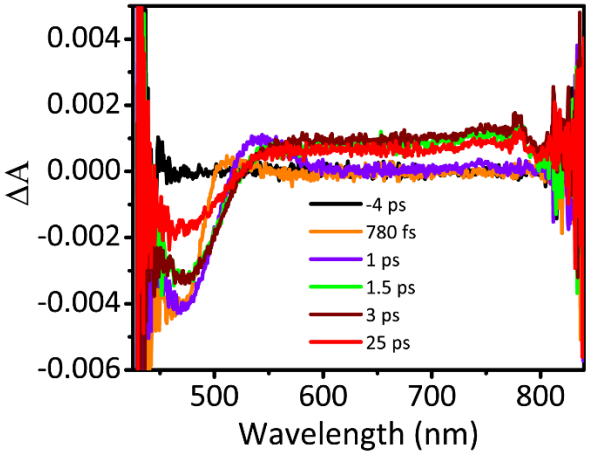

Figure S17. Related to Figure 4. The non-linear absorbance spectroscopy of undoped InP/5 ML ZnSe QDs with the same delays with the doped sample.

References

Anand, A., Zaffalon, M.L., Gariano, G., Camellini, A., Gandini, M., Brescia, R., Capitani, C., Bruni, F., Pinchetti, V., and Zavelani-Rossi, M. (2019). Evidence for the Band-Edge Exciton of CuInS2 Nanocrystals Enables Record Efficient Large-Area Luminescent Solar Concentrators. Advanced Functional Materials *30*, 1906629.

Bakueva, L., Gorelikov, I., Musikhin, S., Zhao, X.S., Sargent, E.H., and Kumacheva, E. (2004). PbS quantum dots with stable efficient luminescence in the near-IR spectral range. Advanced Materials *16*, 926-929.

Bergren, M.R., Makarov, N.S., Ramasamy, K., Jackson, A., Guglielmetti, R., and McDaniel, H. (2018). High-performance CuInS2 quantum dot laminated glass luminescent solar concentrators for windows. ACS Energy Letters *3*, 520-525.

Bomm, J., Büchtemann, A., Chatten, A.J., Bose, R., Farrell, D.J., Chan, N.L., Xiao, Y., Slooff, L.H., Meyer, T., and Meyer, A. (2011). Fabrication and full characterization of state-of-the-art quantum dot luminescent solar concentrators. Solar Energy Materials and Solar Cells *95*, 2087-2094.

Chen, C., He, X., Gao, L., and Ma, N. (2013). Cation exchange-based facile aqueous synthesis of small, stable, and nontoxic near-infrared Ag2Te/ZnS core/shell quantum dots emitting in the second biological window. ACS applied materials & interfaces *5*, 1149-1155.

Coropceanu, I., and Bawendi, M.G. (2014). Core/shell quantum dot based luminescent solar concentrators with reduced reabsorption and enhanced efficiency. Nano letters *14*, 4097-4101.

Erickson, C.S., Bradshaw, L.R., McDowall, S., Gilbertson, J.D., Gamelin, D.R., and Patrick, D.L. (2014). Zero-reabsorption doped-nanocrystal luminescent solar concentrators. ACS nano *8*, 3461-3467.

Klimov, V.I., Baker, T.A., Lim, J., Velizhanin, K.A., and McDaniel, H. (2016). Quality factor of luminescent solar concentrators and practical concentration limits attainable with semiconductor quantum dots. ACS Photonics *3*, 1138-1148.

Li, H., Wu, K., Lim, J., Song, H.-J., and Klimov, V.I. (2016). Doctor-blade deposition of quantum dots onto standard window glass for low-loss large-area luminescent solar concentrators. Nature Energy *1*, 16157.

Ma, W., Li, W., Cao, M., Liu, R., Zhao, X., and Gong, X. (2019). Large Stokes-shift AIE fluorescent materials for high-performance luminescent solar concentrators. Organic Electronics *73*, 226-230.

Meinardi, F., Colombo, A., Velizhanin, K.A., Simonutti, R., Lorenzon, M., Beverina, L., Viswanatha, R., Klimov, V.I., and Brovelli, S. (2014). Large-area luminescent solar concentrators based on 'Stokes-shift-engineered'nanocrystals in a mass-polymerized PMMA matrix. Nature Photonics *8*, 392.

Meinardi, F., Ehrenberg, S., Dhamo, L., Carulli, F., Mauri, M., Bruni, F., Simonutti, R., Kortshagen, U., and Brovelli, S. (2017). Highly efficient luminescent solar concentrators based on earth-abundant indirect-bandgap silicon quantum dots. Nature Photonics *11*, 177.

Meinardi, F., McDaniel, H., Carulli, F., Colombo, A., Velizhanin, K.A., Makarov, N.S., Simonutti, R., Klimov, V.I., and Brovelli, S. (2015). Highly efficient large-area colourless luminescent solar concentrators using heavy-metal-free colloidal quantum dots. Nature nanotechnology *10*, 878.

Nakane, Y., Tsukasaki, Y., Sakata, T., Yasuda, H., and Jin, T. (2013). Aqueous synthesis of glutathione-coated PbS quantum dots with tunable emission for non-invasive fluorescence imaging in the second near-infrared biological window (1000–1400 nm). Chemical Communications *49*, 7584-7586.

Sadeghi, S., Bahmani Jalali, H., Melikov, R., Ganesh Kumar, B., Mohammadi Aria, M., Ow-Yang, C.W., and Nizamoglu, S. (2018). Stokes-Shift-Engineered Indium Phosphide Quantum Dots for Efficient Luminescent Solar Concentrators. ACS Applied Materials & Interfaces *10*, 12975-12982.

Sadeghi, S., Melikov, R., Bahmani Jalali, H., Karatum, O., Srivastava, S., Conkar, D., Firat Karalar, E.N., and Nizamoglu, S. (2019). Ecofriendly and Efficient Luminescent Solar Concentrators Based on Fluorescent Proteins. ACS applied materials & interfaces *11*, 8710-8716 .

Sennaroglu, A., Demirbas, U., Ozharar, S., and Yaman, F. (2006). Accurate determination of saturation parameters for Cr 4+-doped solid-state saturable absorbers. JOSA B *23*, 241-249.

Sharma, M., Gungor, K., Yeltik, A., Olutas, M., Guzelturk, B., Kelestemur, Y., Erdem, T., Delikanli, S., McBride, J.R., and Demir, H.V. (2017). Near-Unity Emitting Copper-Doped Colloidal Semiconductor Quantum Wells for Luminescent Solar Concentrators. Advanced Materials *29*, 1700821.

Slooff, L.H., Bende, E.E., Burgers, A.R., Budel, T., Pravettoni, M., Kenny, R.P., Dunlop, E.D., and Büchtemann, A. (2008). A luminescent solar concentrator with 7.1% power conversion efficiency. physica status solidi (RRL)–Rapid Research Letters *2*, 257-259.

Sumner, R., Eiselt, S., Kilburn, T.B., Erickson, C., Carlson, B., Gamelin, D.R., McDowall, S., and Patrick, D.L. (2017). Analysis of optical losses in high-efficiency CuInS2-based nanocrystal luminescent solar concentrators: balancing absorption versus scattering. The Journal of Physical Chemistry C *121*, 3252-3260.

Tummeltshammer, C., Taylor, A., Kenyon, A.J., and Papakonstantinou, I. (2016). Flexible and fluorophore-doped luminescent solar concentrators based on polydimethylsiloxane. Optics letters *41*, 713-716.

Vinokurov, A., Chernysheva, G., Mordvinova, N., and Dorofeev, S. (2018). Optical properties and structure of Ag-doped InP quantum dots prepared by a phosphine synthetic route. Dalton Transactions *47*, 12414-12419.

Weber, W., and Lambe, J. (1976). Luminescent greenhouse collector for solar radiation. Applied optics *15*, 2299-2300.

Wei, M., de Arquer, F.P.G., Walters, G., Yang, Z., Quan, L.N., Kim, Y., Sabatini, R., Quintero-Bermudez, R., Gao, L., and Fan, J.Z. (2019). Ultrafast narrowband exciton routing within layered perovskite nanoplatelets enables low-loss luminescent solar concentrators. Nature Energy, *4*, 197-205.

Wu, K., Li, H., and Klimov, V.I. (2018). Tandem luminescent solar concentrators based on engineered quantum dots. Nature Photonics *12*, 105.

Xie, R., Chen, K., Chen, X., and Peng, X. (2008). InAs/InP/ZnSe core/shell/shell quantum dots as near-infrared emitters: bright, narrow-band, non-cadmium containing, and biocompatible. Nano research *1*, 457-464.

Xie, R., and Peng, X. (2009). Synthesis of Cu-doped InP nanocrystals (d-dots) with ZnSe diffusion barrier as efficient and color-tunable NIR emitters. Journal of the American Chemical Society *131*, 10645-10651.

Yang, C., Liu, D., and Lunt, R.R. (2019). How to Accurately Report Transparent Luminescent Solar Concentrators. Joule *3*, 2871-2876.

Zhang, Y., Hong, G., Zhang, Y., Chen, G., Li, F., Dai, H., and Wang, Q. (2012). Ag2S quantum dot: a bright and biocompatible fluorescent nanoprobe in the second near-infrared window. ACS nano *6*, 3695-3702.

Zhao, H., Benetti, D., Jin, L., Zhou, Y., Rosei, F., and Vomiero, A. (2016). Absorption Enhancement in "Giant" Core/Alloyed-Shell Quantum Dots for Luminescent Solar Concentrator. Small *12*, 5354-5365.

Zhao, H., Zhou, Y., Benetti, D., Ma, D., and Rosei, F. (2017). Perovskite quantum dots integrated in large-area luminescent solar concentrators. Nano Energy *37*, 214-223.

Zhou, W., Wang, M.-C., and Zhao, X. (2015). The properties of PMMA/DCJTB thin-film luminescent solar concentrator with various thicknesses. Solar Energy *120*, 419-427.

Zhou, Y., Benetti, D., Fan, Z., Zhao, H., Ma, D., Govorov, A.O., Vomiero, A., and Rosei, F. (2016). Near infrared, highly efficient luminescent solar concentrators. Advanced Energy Materials *6*, 1501913.

Zhou, Y., Benetti, D., Tong, X., Jin, L., Wang, Z.M., Ma, D., Zhao, H., and Rosei, F. (2018). Colloidal carbon dots based highly stable luminescent solar concentrators. Nano Energy *44*, 378-387.